

Multi-level Cellular Automata for FLIM networks

Felipe Crispim R. Salvagnini*, Jancarlo F. Gomes*, Cid A. N. Santos[†], Silvio Jamil F. Guimarães[‡],
Alexandre X. Falcão*

*University of Campinas

[†]Eldorado Institute

[‡]Pontifical Catholic University of Minas Gerais

Email: felipe.salvagnini@students.ic.unicamp.br, jgomes@ic.unicamp.br, cid.santos@eldorado.org.br,
sjamil@pucminas.br, afalcao@unicamp.br

Abstract—The necessity of abundant annotated data and complex network architectures presents a significant challenge in deep-learning Salient Object Detection (deep SOD) and across the broader deep-learning landscape. This challenge is particularly acute in medical applications in developing countries with limited computational resources. Combining modern and classical techniques offers a path to maintaining competitive performance while enabling practical applications. Feature Learning from Image Markers (FLIM) methodology empowers experts to design convolutional encoders through user-drawn markers, with filters learned directly from these annotations. Recent findings demonstrate that coupling a FLIM encoder with an adaptive decoder creates a flyweight network suitable for SOD, requiring significantly fewer parameters than lightweight models and eliminating the need for backpropagation. Cellular Automata (CA) methods have proven successful in data-scarce scenarios but require proper initialization — typically through user input, priors, or randomness. We propose a practical intersection of these approaches: using FLIM networks to initialize CA states with expert knowledge without requiring user interaction for each image. By decoding features from each level of a FLIM network, we can initialize multiple CAs simultaneously, creating a multi-level framework. Our method leverages the hierarchical knowledge encoded across different network layers, merging multiple saliency maps into a high-quality final output that functions as a CA ensemble. Benchmarks across two challenging medical datasets demonstrate the competitiveness of our multi-level CA approach compared to established models in the deep SOD literature.

Index Terms—SOD, Cellular Automata, Multi-Level Cellular Automata, Cellular Automata Ensemble, Saliency Merging, Feature Learning from Image Markers, FLIM, Adaptive Decoders.

I. INTRODUCTION

When a specialist analyzes an image, such as a neuroradiologist investigating tumors in patients' Magnetic Resonance Imaging (MRI) data, abnormalities usually stand out and are easily spotted. Likewise, a parasitologist can quickly locate parasite eggs in microscopic images. In some images, even someone without training can identify the abnormalities. Additionally, we naturally perform this task when we observe a scene and the foreground becomes prominent. Salient Object Detection (SOD) methods propose to tackle the same problem, generating a saliency map where the foreground (or abnormality) is brighter than the background.

SOD methods are categorized into bottom-up or top-down approaches [Qin et al., 2018]. Bottom-up methods employ low-level features — local properties such as color, texture, and descriptors — and statistics to identify foreground regions [Tong et al., 2015]. Conversely, top-down techniques utilize high-level features extracted through supervised methods, which require annotated data [Qin et al., 2019, 2020; Zhu et al., 2024]. Some works also categorize those approaches into traditional manual feature learning and deep-learning-based methods [Yang et al., 2025].

Despite the recent success of deep-learning approaches applied to SOD, as models get even more sophisticated, they face two-main challenges under real-world applications: the demand for high-cost computational resources (GPUs) and the requirement of many annotated data (even when pre-trained). The literature proposes to solve the former through *Lightweight Models*, where the complexity of the models is reduced by the model's design or compression [Chen et al., 2024]. Although they speed up inferences and reduce model size, lightweight models still have around 1 million to 5 million parameters and require a large amount of annotated data.

The FLIM methodology tackles deep-learning challenges by enabling us to design flyweight convolutional networks (usually 2 to 5 layers) under expert control [Joao et al., 2023]. Flyweight is a term that describes networks even lighter than lightweight models, with around 500k parameters. Inserting a user in the interactive pipeline enables: (1) Selection of representative images (usually less than 10) [Cerqueira et al., 2024b]; (2) Design of a convolutional encoder from weak annotations inserted by a user (*e.g.*, scribbles or disks) [Salvagnini et al., 2024; Soares et al., 2024]; (3) Get the saliency map by adaptively decoding features extracted by the encoder [Soares et al., 2024]. FLIM is a recently proposed method, and each of those three steps is under investigation.

FLIM networks are suitable for data-scarcity scenarios where the entire network is backpropagation-free. Hence, there is no requirement for densely annotated ground truth, only weak annotations on a few images. Such an approach is not data-hungry and employs learned high-level features to generate saliency maps. The saliency map generated by FLIM is particularly suitable to initialize a bottom-up method. The latter behaves as a post-processing operation, where we take advantage of low-level and high-level features.

Cellular Automata (CA) methods present an excellent candidate for integration with FLIM networks as a post-processing mechanism, where FLIM networks can significantly enhance the initialization phase. CA is commonly applied to data-scarce scenarios (*e.g.*, medical images), where the CA is executed for each input. CA also enables SOD methods using both low-level [Vezhnevets and Konouchine, 2005; Hamamci et al., 2012] and high-level features [Qin et al., 2018, 2015]. Nevertheless, CA methods require proper initialization. Common strategies are: initialize states from user inputs like a line drawn on image regions [Vezhnevets and Konouchine, 2005; Hamamci et al., 2012; Sompong and Wongthanavas, 2017b]; random initialization [Marinescu et al., 2018]; priors (as background or contrast priors) [Qin et al., 2018]. As far as we are concerned, no work takes advantage of high-level features during initialization; only user-based methods employ the expert’s knowledge but require the user for every inference image. Therefore, investigating FLIM for CA initialization is of particular interest.

The meeting of FLIM networks with CA enables a novel initialization technique, characterized by three phases: (1) Design of a FLIM Encoder, which together with an adaptive decoder yields a FLIM network; (2) at inference time initialize CA using a FLIM-Network saliency; (3) evolve the CA to generate a better saliency map. **The key aspect is, unlike other user-interaction-based SOD methods, user interaction is not required at inference time.**

Our previous research investigated the initialization of CA using FLIM networks [Salvagnini et al., 2024]. Specifically, with an L -layer FLIM encoder, we decoded feature maps from the last convolutional layer into a saliency map to initialize the CA. As established in [Salvagnini et al., 2024] and reiterated here, FLIM encoders detect descriptive and discriminative patterns beginning from the first layer. The initial layers activate strongly in edge regions, providing sharp features but generating numerous false positive activations. In contrast, deeper layers produce fewer or no false positives, though they yield blurrier activations in edge regions. These complementary characteristics suggest the value of decoding saliency maps from each FLIM-Encoder level to initialize multiple CA simultaneously. This multi-level initialization approach enables exploring a broader initialization space, combining the precision of early layers with the reliability of deeper representations, better exploring the edge and internal regions of the salient objects. Moreover, this novel method, called multi-level CA, opens room for investigation on combining the saliency of multiple CAs, which can be seen as an ensemble of CA models.

In improving our previous study, this work investigates the applicability and generalization of our multi-level CA towards two challenging datasets: brain tumors (glioblastomas) and parasite eggs (*Schistosoma Mansonii*) detection. It evaluates the proposed method towards gray-scale MRI images — with high heterogeneity from multiple institution acquisitions [Baid et al., 2021] — and RGB microscopy images [Suzuki et al., 2013]. Our main contributions are:

- 1) We demonstrate significant performance enhancements by initializing multi-level CA with saliencies from each level of the FLIM network. Measurable improvements are observed across each hierarchical layer;
- 2) We extend compassion to SOD literature to include lightweight models to address the criticality of deploying salient object detection in low-cost devices;
- 3) We propose a simple yet elegant fusion mechanism — only three convolutional filters — that effectively integrates multi-level saliency maps into a final saliency. Our experimental results show that our method achieves comparable performance or even surpasses specialized lightweight models and state-of-the-art deep learning SOD architectures (pre-trained on thousands to millions of images).

This work is organized as follows: Section II provides a comprehensive review of SOD literature, covering both classical bottom-up models and modern top-down deep learning approaches. Additionally, it introduces the FLIM methodology and explores CA applications in both SOD and semantic segmentation problems, establishing the foundation necessary for understanding our proposed method. Section III presents our multi-level CA method in detail, examining the integration of FLIM networks into hierarchical CA initialization, the CA evolution process, and the ensemble technique that combines multiple CAs to yield enhanced saliency maps. Section IV describes our experimental setup, guiding the reader through creating a multi-level CA. At the same time, we also discuss the methodology for benchmarking our approach against state-of-the-art methods. Section V thoroughly discusses our results across each stage of the proposed method. Finally, Section VI concludes with our findings, acknowledges the limitations of our approach, and outlines directions for future research.

II. RELATED WORKS

This section reviews the bottom-up and deep-learning SOD methods and builds the intuition behind FLIM methodology and Cellular Automata, setting the foundation for our approach.

A. Bottom-up methods

Bottom-up methods are rooted in cognitive psychology and human perception to predict which areas of an image capture people’s attention [Itti et al., 1998]. This process typically consists of two stages: first, identifying the region that stands out, and then accurately segmenting that region by fitting a saliency map to the object’s interior and edges [Borji et al., 2019; Wang et al., 2022; Zhu et al., 2024].

These classical methods operate directly on low-level features, such as image intensity, color, contrast, and gradients [Itti et al., 1998; Wang et al., 2024]. Hence, they do not need to learn semantic information, alleviating the requirement for abundant training data. Intrinsic features (derived from the image itself) and/or extrinsic features (*e.g.*, statistics from images or user interaction) are employed, where computational

heuristics or classical supervision techniques yield the final saliency map.

Itti et al. [1998] drew attention to the topic by taking inspiration from the efficiency of primates’ visual mechanism for complex scene understanding. Their seminal work operates over colors, intensity, and orientations at multiple scales (*i.e.*, gaussian pyramids) to generate a salience map. The first SOD models were based on local contrast — the difference between a pixel, or a patch, and its neighbors — to compute salient regions [Ma and Zhang, 2003; Liu and Gleicher, 2006; Liu et al., 2007a; Achanta, Radhakrishna et al., 2008; Rosin, 2009].

For example, Ma and Zhang [2003] employs a perceive field (same size as the input image), where each pixel is a perception unit operating on a neighborhood, measuring the contrast as the color distance in LUV space. This local contrast saliency map is then processed by a region-growing process (fuzzy growing), which splits the pixels into two classes: attended or unattended areas. Liu et al. [2007a] further expands by applying Conditional Random Field (CRF) learning to combine local, regional, and global features: multi-scale contrast, center-surround histogram, and color spatial distribution. Achanta, Radhakrishna et al. [2008] adds and normalizes multi-scale saliency map, where a thresholded image generates the salient object map. Later, Rosin [2009] improves the use of image features by applying edge detection, threshold decomposition, and distance transformation [Borgefors, 1984]. Remarkably, most of the preliminary works on the field employed intrinsic features (input image only) and center-pixel neighborhoods despite being computed at multiple scales.

Other works then explored whole image regions, such as the work of Liu and Gleicher [2006], where a hybrid approach first extracts an intermediary saliency using contrast and later improves by averaging the saliency value of the image’s regions, where the mean shift image segmentation algorithm extracts the regions. Another example is the work of Cheng et al. [2015a], which efficiently computes pixel-level global contrast (using a global histogram) and later improves the intermediary results with a region-level analysis and spatial weighting. This work extracts regions using Felzenszwalb and Huttenlocher’s segmentation method [Felzenszwalb and Huttenlocher, 2004]. Concurrently, as more images became available, researchers began incorporating extrinsic features, enabling salient object detection methods to leverage similar images as references to generate saliency maps [Wang et al., 2011].

A deeper review of SOD literature will also reveal that some assumptions improve the overall results. As is the case of *background prior* — assuming that pixels/blocks/regions at the image frame are the foreground, or conversely the *center prior*. However, they do not stand for all categories of images (*e.g.*, parasites in microscopy images can appear near the image’s frame). For readers seeking a more comprehensive review of the techniques employed by bottom-up methods, we strongly recommend the survey conducted by Borji et al. [2019].

Nevertheless, despite the vast amount of bottom-up meth-

ods, the literature has consistently struggled with a critical weakness: poor generalization. As most approaches rely on low-level and hand-crafted features, applying them to different domains was highly challenging, particularly in complex scenes. The emergence of CNNs promoted a significant shift in the field, as researchers began leveraging deep learning ability to automatically extract and integrate low-level and high-level semantic features, producing more accurate and robust saliency maps across diverse visual contexts.

B. Deep Learning & Lightweight models

Categorized as top-down approaches, deep-learning-based SOD methods (*deep SOD*) focus on learning high-level semantic features, commonly through supervision. Deep SOD employs an encoder that learns both low-level (*e.g.*, edges, corners) and high-level features (*e.g.*, complex textures, shapes) and, subsequently, a decoder that combines extracted features into a saliency object map — the pixel-wise prediction of the most visually important objects in the scene — with the size of the input image [Zhu et al., 2024].

Since 2015, when deep SOD was introduced, the majority of works in the field apply Deep Neural Networks (DNNs) to explore local and global features [Wang et al., 2015; Li and Yu, 2015; Zhao et al., 2015]. Classical methods in the past had struggled in both tasks, where methods based on local features are usually better at detecting salient objects’ edges than their interior; conversely, global methods do not perform well when the object’s textures are similar to the background.

Building this evolutionary shift in SOD methodology, Wang et al. [2015] proposed a saliency detection approach called LEGS (Local Estimation and Global Search) utilizing two deep-neural networks (DNNs), a local (DNN-L) and a global one (DNN-G). DNN-L focuses on local features, classifying a central pixel (of a 51×51 patch) as salient/non-salient. DNN-L is applied to the input image through a sliding window at inference and later refined through geodesic object proposal. Globally, a feature vector describes each region’s global contrast, geometric information, and local saliency measurements (from DNN-L). DNN-G gets the global feature vector of each region as input and outputs the region’s salient value, which is further sorted and yields the final saliency map through a weighted sum of the top K candidate masks. DNN-L comprises convolutional, max-pooling, and fully connected layers, while DNN-G is built only with fully connected layers.

In addition to exploring local and global features, the work of Li and Yu [2015] proposes a multiscale approach using CNN features. Employing a neural network architecture with fully connected layers on top of CNNs, they extract features at three different spatial scales, generating saliency maps at different scales, which are then linearly combined. A key innovation was leveraging convolutional weights pretrained on the ImageNet dataset, enabling rich semantic understanding for visual saliency detection. Similarly, Zhao et al. [2015] also employed a single network to derive a saliency map, but through a dual branch architecture, a local-context branch and a global-context branch, which outputs are employed to

classify a super-pixel (the super-pixel's center is the network's input) as salient/non-salient. They also carried out a more in-depth analysis of using pre-trained models.

The onset of larger datasets also played a central role in deep-learning adoption, such as MSRA-5000 [Liu et al., 2007b], SOD [Movahedi and Elder, 2010], ECCSD [Yan et al., 2013], PASCAL-S [Li et al., 2014], MSRA10K [Cheng et al., 2015b], and DUTS [Wang et al., 2017].

The seminal deep-SOD's works based on multi-layer perceptrons (*i.e.*, fully connected layers) took advantage of image subunits and object proposals [Wang et al., 2015]. Image subunits are super-pixels and patches, while between examples of object proposals, we could cite regions, as the work of Wang et al. [2015], and bounding-boxes. Those subunits are then scored as salient/non-salient. Despite outperforming bottom-up approaches, these methods cannot fully explore spatial information and are time-consuming (*i.e.*, running for all image subunits at inference time).

To tackle the aforementioned problems of representation learning and inference time, the literature employed fully convolutional networks (FCN) [Liu and Han, 2016]. FCNs enable a single model capable of learning multi-level features simultaneously, which better explores spatial information. Furthermore, FCNs operate over the whole input image, requiring a single feed-forward process, significantly speeding up inferences. The seminal work of Liu and Han [2016] proposed the DHSNet (Deep Hierarchical Saliency Network), which is composed of a two-step architecture. First, they coarsely detect salient objects from a global perspective (VGG Convolutional encoder), and then, through recurrent convolutions, they refine the details of the saliency map in a step-by-step fashion.

Recent SOD models further explore multi-scale feature extractions to improve results and also loss functions to better guide the representational learning phase. Great examples are the works of Qin et al. [2019, 2020], which proposes the BasNet and U²-Net architectures. BasNet is a deeply supervised encoder-decoder (*i.e.*, it employs deep supervision, computing loss, and backpropagating errors for each decoder level) [Qin et al., 2019]. Its weights are learned through a hybrid boundary-aware loss to learn at pixel, patches, and map levels (*i.e.*, BCE, SSIM, and IoU, respectively). Extending this approach, U²-Net takes advantage of nested U-shaped architectures to improve high-level feature extraction at multiple resolutions (intra-stage multi-scale features) [Qin et al., 2020].

Still, there is an ongoing trend to enhance model architecture for better extraction of features at multiple scales. A good example is the work of Huang et al. [2023], which proposes the Multilevel Diverse Feature Aggregation Network (MDFNet), composed of different modules to capture saliency information at multiple directions and channels, learn correlation of different salient objects, improve extraction of boundary information. The proposed method combines multilevel features and detects suitable feature spaces and channels for better saliency maps. Although this trend yields models suitable for complex scenarios, the downside is higher complexities and, consequently, high inference time.

The problem of high inference time is worst in scenarios where computing resources are limited, such as our problem of detecting parasite eggs in a tropical country (*e.g.*, Brazil), where laboratories usually do not have computers with GPUs. To address this issue, one could refer to literature on lightweight models concerned with lowering hardware requirements and speeding up inferences with competitive performance [Chen et al., 2024]. The first approach to generate a lightweight model focuses on architecture design, where fewer model parameters and computational complexity are possible through convolution paradigms (*e.g.*, dilated separable convolutions [Liu et al., 2021] and depth-wise convolutions [Sandler et al., 2018]) or AutoML [Chu et al., 2020]. On the other hand, the second approach employs model compression by optimizing larger models through model pruning, quantization, knowledge distillation, or low-rank decomposition [Phan et al., 2020; Chariton et al., 2022; Huang et al., 2024]. Despite those efforts, lightweight models still have around 1M to 5M parameters and require considerable training data. Furthermore, under constrained scenarios, high inference times are still prohibitive (*e.g.*, running for a slicing window of a microscopy slide).

To summarize, key questions remain for deep SOD models, mainly in scenarios where we do not have large annotated datasets and inference time is mandatory. Related to datasets, when few annotated data are available, how can we efficiently train a network? Should we consider training from scratch, or would transfer learning be a more practical approach? Regarding the model architecture, how can we discover the lightest network that can solve our problem? How many convolutional layers are required? And the correct number of filters? Those questions permeate not only the deep SOD field but deep learning in general.

C. Feature learning from Image Markers

Over recent years, works employing the FLIM methodology have consistently demonstrated comparable and even superior results under a data scarcity regime [Joao et al., 2023; de Souza and Falcão, 2022; de Souza et al., 2020]. Such scenarios are particularly challenging to deep-learning models. Deep SOD models commonly overfit and do not generalize to unseen data when learning with little data. For instance, in Wang et al. [2022], they argue that SOD methods struggle when applied to unseen datasets, even if trained with thousands of data. Hence, at least fine-tuning deep SOD methods towards the target task is a must, but learning a different domain is still a problem.

The FLIM methodology (Figure 1) is a recently proposed approach [de Souza et al., 2020], which is under active investigation. It integrates user knowledge into the design of a feature extractor (*i.e.*, a convolutional encoder). User knowledge is exploited in different methodology phases, encompassing the selection of training images, identification of discriminative regions for filter estimation, and filter evaluation and selection. The methodology allows the design of a CNN encoder layer by layer. The user can create the encoder architecture by selecting

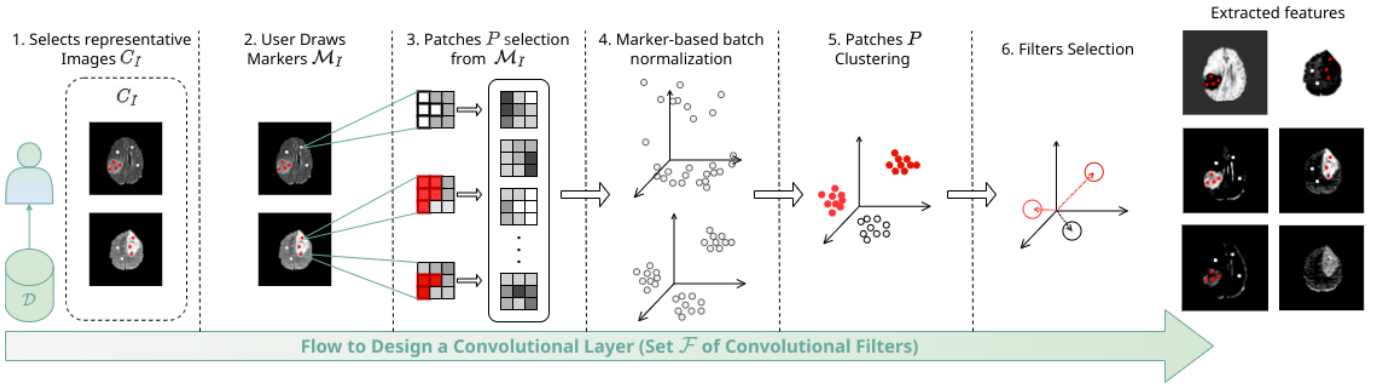


Fig. 1: Multi-Level Cellular Automata for FLIM networks: (1) Users iteratively select training images and define FLIM-Encoder architecture. (2) During inference, images enter the encoder, and features decode into intermediary saliency maps, initializing CA cells. (3) Multi-level saliency maps evolve from this initialization, and (4) merge into a final saliency.

representative images and drawing markers on descriptive and discriminative image regions. Conventional filters are then directly estimated from marked regions. Each FLIM encoder holds operations like marker-based normalization, the convolution with a filter bank, the activation function (e.g., ReLU), and pooling (e.g., max-pooling or averaging pooling). All operations, except marker-based normalization, are well-known in the literature. However, the below definition and geometrical interpretation in light of the FLIM methodology provide vital insights.

Let $\mathbf{I} = (D_I, \vec{I}) \in \mathcal{D}$ be an m -channel image from dataset \mathcal{D} , where $D_I \subset \mathbb{Z}^2$ is the image domain and $\vec{I}(p) \in \mathbb{R}^m$ assigns feature values to pixel $p \in D_I$. A patch vector $\vec{P}_p \in \mathbb{R}^{k \times k \times m}$ vectorizes features in a $k \times k \times m$ square region centered at p . The same holds for grayscale ($m = 1$), color ($m = 3$), and feature maps ($m \geq 1$) from filter bank convolutions. It is important to understand that in Figure 1 we represented the FLIM’s filter estimation and extracted features given an image as input (first convolutional layer). However, the input features from past layers and markers are projected into the feature space for deeper layers, so filters are learned directly from features.

The selection of training images is possible through multiple approaches: (1) random selection of a fixed number of images, (2) comprehensive dataset inspection to identify representative images — as demonstrated in our previous research [Salvagnini et al., 2024] —, or (3) iterative selection using validation metrics to build the training set progressively. We implemented the iterative approach in this work, although recent studies have demonstrated the effectiveness of supervised and unsupervised techniques for training image selection [Cerqueira et al., 2024a,b]. This step yields a subset $C_I \subseteq \mathcal{D}$ (usually, $|C_I| \ll |\mathcal{D}|$) of a few representative images.

Given C_I , users mark discriminative regions (disks, scribbles) on each image $\mathbf{I} \in C_I$ while specifying architectural parameters—including filter counts per marker and image, and the target kernel bank size. This process extracts overlapping patches from marked regions, creating a set \mathcal{M}_I of patch

vectors \vec{P}_p for pixels p marked in image \mathbf{I} . These user interactions, required only for training images, demand domain knowledge of both \mathcal{D} and the application context.

With $\mathcal{M} = \bigcup_{\mathbf{I} \in C_I} \mathcal{M}_I$, patch vectors in \mathcal{M} are normalized by z-score, and these normalization parameters are applied to all patch vectors from any image $\mathbf{I} \in \mathcal{D}$. This *marker-based image normalization* centralizes the dataset \mathcal{M} and corrects distortions along the main axes of $\mathbb{R}^{k \times k \times m}$.

For each marker, the user specifies n filters, and k-means clustering of normalized patch vectors produces n clusters whose centers define kernel weight vectors $\vec{K}_i \in \mathbb{R}^{k \times k \times m}$. These kernels compose the filter bank, which may require further reduction (via k-means or PCA) if the total filter count exceeds target layer specifications or the number of filters by image. Convolutioning a normalized image \mathbf{I} with kernel \vec{K}_i produces an image \mathbf{J} where $J_i(p) = \langle \vec{P}_p, \vec{K}_i \rangle$. With a filter bank $\{\vec{K}_i\}_{i=1}^{n \times M}$ from M markers and n filters per marker, $\mathbf{J} = (D_J, \vec{J})$ becomes a feature map with $n \times M$ channels and $\vec{J}(p) = (J_1(p), J_2(p), \dots, J_{n \times M}(p)) \in \mathbb{R}^{n \times M}$.

Geometrically, each kernel \vec{K}_i represents a vector normal to a hyperplane through the origin of $\mathbb{R}^{k \times k \times m}$. The patch vector \vec{P}_p exists as a point in this space, with $J_i(p)$ measuring the signed distance from this point to the hyperplane—positive or negative depending on which side the point falls. ReLU operations remove points on the negative side, while max-pooling consolidates nearby activations. Enforcing unit norm $\|\vec{K}_i\| = 1$ across all kernels prevents $J_i(p)$ amplification by kernel magnitude. The marker-based normalization eliminates bias by centering clusters around the origin of $\mathbb{R}^{k \times k \times m}$.

The operations described so far—patch extraction, marker-based normalization, and subsequent clustering for filter estimation from cluster centers—will repeat until the whole encoder architecture is designed. Layers other than layer one will use feature maps of the previous layer (extracted from C_I images) and project markers into the features’ domain. At this point, we have a FLIM encoder suitable for extracting feature maps for any image in \mathcal{D} .

A key property of FLIM encoders highlighted in Joao et al.

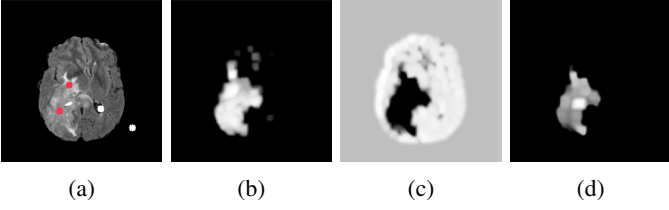


Fig. 2: Adaptive decoder for FLIM-Encoder layer 3 (same across all l layers): (a) input with foreground/background markers; (b) channel i with $w_i = 1$ (foreground); (c) channel j with $w_j = -1$ (background); (d) resulting saliency map \mathcal{S}_3 .

[2023] involves foreground-background differentiation. When markers are placed in distinct regions (Figure 2a), the resulting feature maps show channel-specific activation patterns for either foreground or background elements (Figures 2b-2c). For each layer l in L (total encoder layers), saliency maps \mathcal{S}_l can be generated by applying a weighted channel averaging followed by activation function ϕ (Figure 2d). Optimal saliency maps with enhanced object visibility result from decoders assigning positive weights to foreground channels and negative weights to background channels, eliminating false positives from foreground maps. Since channel weight polarity varies with input images, adaptive decoders become necessary. The work of Joao et al. [2023] presents dataset-specific adaptive decoders, but we will follow with a modified version from Joao. et al. [2024], employed in our previous work [Salvagnini et al., 2024], that aligns with our requirements for saliency map \mathcal{S}_l estimation (Equation 1), where

$$\mathcal{S}_l(p) = \phi(\langle \vec{J}_l(p), \vec{w} \rangle), \quad (1)$$

where $\vec{w} = (w_1, w_2, \dots, w_{n \times M})$, $\vec{J}_l(p)$ is the feature vector at position p for layer l , and ϕ is a given activation function (e.g., ReLU). Each feature map channel weight is estimated as $w_i \in \{-1, 0, 1\}$, by

$$w_i = \begin{cases} +1, & \text{if } \mu_{J_i} \leq \mathcal{T} - \sigma^2 \text{ and } a_i < A_1, \\ -1, & \text{if } \mu_{J_i} \geq \mathcal{T} + \sigma^2 \text{ and } a_i > A_2, \\ 0, & \text{otherwise.} \end{cases} \quad (2)$$

At this point, we have a FLIM network trained without backpropagation and consequently without requiring many pixel-wisely annotated ground truths. We can now run it in inference for training, validation, and testing images and extract saliency maps at any encoder level (*i.e.*, layer).

D. Cellular Automata

First introduced in 1951 by John Von Neumann [von Neumann, 1951], Cellular Automata (CA) — or Cellular Automaton in singular — refers to a discrete evolving model capable of mapping complex behaviors through relatively simple evolution rules. At its core, a CA consists of a regular arrangement of cells, typically organized in a lattice structure. Common examples include grids of cells (analogous to pixels) for 2D images or cubes of cells (similar to voxels) for 3D images. Nevertheless, cells can have formats other than

squares and cubes, as complex surfaces can be represented by irregular tessellations such as Voronoi diagrams or super-pixels [Qin et al., 2015]. This adaptability, combined with the ability to model local iterations, which produce global emergent patterns, is suitable for SOD, where identifying visually distinct regions requires both local contrast analysis and global contextual understanding. Hence, by combining CA with FLIM networks, we create a hybrid approach suitable to tackle SOD challenges, where a FLIM network (FLIM convolutional encoder + adaptive decoder) initializes the CA. Thus, this approach leverages both the hierarchical feature learning capabilities of a FLIM network and the iterative, rule-based refinement of a CA.

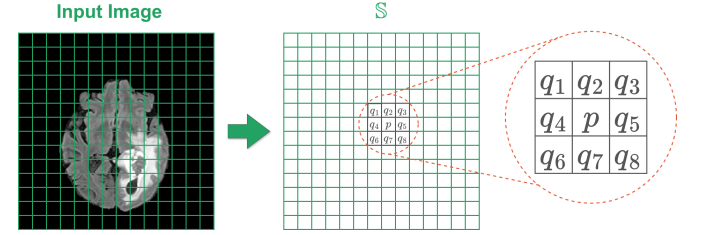


Fig. 3: Brain image as a CA’s lattice of cells, showing individual cells and their neighboring relationships.

When operating over images, the CA requires a set D_I , representing the image domain containing all cells (lattice of cells). Accordingly, we define the CA as a triple (\mathcal{S}, N, δ) , which operates over the lattice of cells, dictating changes over time given each cell’s state \mathcal{S}_p based on the cells’ neighborhood $N(p)$ and a defined local transition function $\delta : \mathbb{S}_p^t \rightarrow \mathbb{S}_p^{t+1}$. The cell’s state evolves through discrete time steps t , where the state of a cell p at time $t + 1$ depends on the configuration of states in its neighbors $N(p)$ at time t . Common neighborhoods are Von Neumann (4-neighbors) and Moore (8-neighbors).

CA applications on images range from classical image processing operations to more complex image analysis tasks. For example, in Hernández and Herrmann [1996], they show the application of CA towards sharpening and smoothing operations, establishing that CA’s methods can converge fast and are also stable in the presence of noise, hence proposing CA as a first-level elementary image enhancement technique. They also discuss the inherently parallel nature of CA and demonstrate results on 2D-Images comparable to widely used software back then, without requiring a priori information. Fast forwarding some years, Rosin [2006] further experimented with CA over additional operations — noise filtering, thinning, and convex hulls — applied on binary and grayscale images. Additionally, the main focus of their work was to draw a method to enable easy training CA, which means designing a set of rules to compose the transition function δ . The authors discuss how even simple rules, combined with a matrix of cells with only local iterations, drive the system to map sophisticated global behaviors.

Then, building upon fundamental image processing tech-

niques, other works have pushed CA applications to SOD. As a more complex task, SOD involves visual understanding and not only pixel-wise transformation (but local and object-level understanding). A seminal CA-SOD method is the work of Qin et al. [2015], where they propose two CA as a post-processing operation capable of improving prior maps from all state-of-the-art methods back then. First, the authors argue that most SOD works take advantage of background priors, which means considering image boundaries as background. Despite this assumption holding for most images, the whole method will generate a wrong saliency when the assumption fails. Hence, to overcome this issue, they begin by segmenting the input image into N small super-pixels — using the SLIC algorithm [Achanta et al., 2012] — described by their mean color features and coordinates. Through the K-means algorithm, boundary super-pixels are then clustered into K clusters based on the CIE LAB color feature. Background seeds are computed from clustered super-pixels by combining geodesic and color information. Once background seeds are available, they evolve it using CA. Their approach considers each super-pixel as a cell, and each cell has as neighbors the adjacent super-pixels and cells with shared boundaries with the adjacent cells. An impact factor matrix and a coherence matrix then drive evolution, where the impact factor matrix measures the similarity in the CIE LAB color space between every cell, and the coherence matrix assesses the level of agreement between the state of the cell and its neighbors. As a last contribution, they propose a multi-level cellular automaton, which combines multiple state-of-the-art methods’ saliency maps to generate a final saliency map. In this Multi-layer CA, each cell represents a pixel. Moreover, unlike the Single-layer CA, neighborhoods are defined across saliency maps rather than within a single map - specifically, pixels with the exact coordinates in different saliency maps are considered neighbors. They demonstrated results surpassing the current methods through a Bayesian framework, with their approach effectively integrating the complementary advantages of different SOD methods.

Additionally, Qin et al. further contributed to the field by exploring a hierarchical CA towards SOD [Qin et al., 2018], again using a single- and a multi-level CA. This time, they extracted super-pixels for different image scales and deep features — extracted using FCN-32s [Shelhamer et al., 2017] — to guide evolution.

Semantic segmentation, another closely related image analysis domain where CA has been successfully applied, shares significant methodological overlap with SOD, where semantic segmentation is also concerned with classifying image pixels. However, it classifies every pixel/voxel between N classes (e.g., health tissue/tumor tissue), where SOD only concerns detecting the most salient object of the scene (e.g., tumor tissue). Nevertheless, given the overlapping between the fields, we can drive inspiration from CA for semantic segmentation, mainly when applied to medical image analysis.

For example, in Vezhnevets and Konouchine [2005], the authors proposed a CA algorithm for semantic segmentation called GrowCut. Given an N -dimensional image as a lattice

of cells, they describe each cell by a triple (lb, θ, \vec{C}) , where lb is the label of the cell, θ the strength, and \vec{C} the RGB vector. Then, the user initializes seed cells by adding markers on images with labels (e.g., background or foreground, or more classes); simultaneously, the cell’s strength (θ) is initialized. From these segmentation seeds, evolution happens, where the neighbors attack cells at each iteration. The attack force is controlled by the cell strength weighted by a monotonous decreasing function, which computes the distance between RGB vectors. If an adjacent cell has a higher strength value and is very similar to the central cell, it will conquer the central cell. Moreover, they also enable boundary smoothness by adding the concept of enemies (surrounding cells with different labels). Thresholding the number of enemies, they forbid cells to attack or conquer them automatically. Following the same trend, Kauffmann and Piché [2010] explores seeded algorithms but embeds the Ford-Bellman algorithm as an evolution rule using GPU optimization. From K labeled seeds, initialized by a user, they evolve the CA to compute multiple shortest-path trees. Once CA converges, K -cuts generate the final segmentation. Most interestingly, the authors integrate medical experts in the tests and show competitive performance (on low-cost graphics hardware suitable in 2010) for clinical routine. The possibility of implementing algorithms through CA is particularly interesting, as there is evidence that a CA with the proper rules can emulate a universal Turing machine and, therefore, implement anything computable [Cook et al., 2004]. Thus, it is possible to implement a more complex algorithm through carefully designed rules and parallelize it (given the characteristics of straightforward parallelization for CA).

The GrowCut algorithm was then adapted towards brain tumors in Hamamci et al. [2012] through the Tumor-Cut algorithm. Considering the characteristic necrotic core of brain tumor MRI images, they propose a two-step method, where the whole tumor is first segmented. Then, the necrotic core is segmented through a CA-based approach. This time, user input must be a line drawn over the largest visible diameter of the tumor, which initializes cells with labels and strengths for the foreground (tumor). Additionally, it generates a volume of interest (VOI) over a sphere, which is 35% larger than the drawn line. The VOI’s border then initializes the background’s labels and strengths. By evolving the foreground and background strengths, a tumor probability map is then calculated, which is used to evolve a level set surface to impose spatial smoothness, generating the final tumor segmentation. The necrotic core is segmented by computing two thresholds, one for necrotic voxels and the other for enhanced voxels. These thresholded voxels are initial seeds for a cellular automata algorithm that labels the remaining mid-intensity voxels. Years ago, the tumor cut algorithm was expanded to consider a second-order statistic (gray-level co-occurrence matrix) to evolve CA [Sompong and Wongthanavas, 2017a].

Despite further modifications, all methods derived from GrowCut share the same evolving characteristic: a cell q propagates its state to a cell p at time $t + 1$ if both p and q cells are similar (close pixel color, intensity, or features) and if

q has more strength than p given the monotonous decreasing function g , which means $g(p, q) \times \theta_{lb}^t(q) > \theta_{lb}^t(p)$.

As a review of both SOD and segmentation methods reveals, CA enables applications on both natural and medical images. Nevertheless, most works initialize the CA by user interaction, which is acceptable for a few images but is burdensome, costly, and error-prone under scenarios where running for many images is mandatory. Given the works on FLIM previously discussed, the possibility of integrating FLIM networks with CA initialization arises. Interestingly, we can CA by employing previous user knowledge without requiring user interaction for every image. Hence, initializing CA employing a FLIM network is of particular interest.

III. MULTI-LEVEL CELLULAR AUTOMATA

Our method leverages the FLIM methodology to address the limitations of deep SOD literature. Figure 4 illustrates our proposed method implemented through a 4-level FLIM network, though the framework is adaptable to FLIM architectures with any number of layers (L). This section details each step of our method. First, we will approach the design phase, guiding the reader through selecting images and defining the architecture of a FLIM encoder. Then, we address how the decoded features are employed to initialize the CA's states. Once the multi-level CA are initialized, we will detail how they evolve and yield a probability map. Ultimately, we will detail an approach to merge multiple CAs' output.

A. Design phase

The design phase focuses on training a FLIM Convolutional Encoder, the core component of the FLIM network. This first step is the only stage in our method that requires user interaction, which occurs in two specific, well-defined steps: First, as discussed in Section II-C, the user selects a set of representative images (C_I) following an iterative procedure. Second, given the selection of an initial image, the user places markers (dots) in descriptive and discriminative image regions. Figure 5 shows two examples of user makers inserted on selected images.

The designed FLIM encoder is then combined with the adaptive decoder (Equation 1), which generates saliency maps for each network layer, such as $S_l = \{S_l\}_{l=1}^L$, in which L is the number of layers of the convolutional encoder. Then, the quality of saliency maps is assessed on a validation subset. The worst cases on validation may be selected to compose the training data, repeating the previous two steps. The iterative procedure is then stopped when acceptable performance is achieved, and this usually happens around 3 to 4 images for the evaluated datasets. Additionally, to supervise which image regions compose the convolutional filters, the user has complete control of the encoder's architecture through a configuration file.

B. CA's initialization

Once we train the FLIM encoder, we can extract features at each encoder level by feeding it an input image. User interaction is only needed during the design phase. Now, the FLIM

encoder is run in inference mode for remaining validation (excluding training images) and test images; validation is used to guide CA parametrization and test to assess our method. We then sequentially decode features at each level, generating an intermediate saliency map to initialize the state of the CA. Combining the FLIM encoder and adaptive decoders forms a *FLIM network* [Soares et al., 2024; Salvagnini et al., 2024], an architecture designed for extracting saliency maps. This L -layers network is developed end-to-end without requiring backpropagation and eliminates the need for pixel-wise annotated ground truths.

The CA's initialization corresponds to the second block in Figure 4, exemplified for a 4-layer FLIM network towards parasite egg detection; nevertheless, the method is suitable for encoders with any number of layers. We decode each encoder's features and generate an intermediary saliency map for each encoder level. Consequently, we generate a set of L intermediary saliency maps: $S_l = \{S_l\}_{l=1}^L$. Each intermediary saliency map initializes one CA, which represents a significant improvement over our previous work by leveraging the delineation-to-detection capability of FLIM-Networks (see Figures 14b to 14e). Using each FLIM network level, we can initialize multiple Cellular Automata (CAs)—one for each network layer—which expands our initialization space. This multi-level CA approach better captures both edge and internal regions of salient objects while effectively reducing false positives (see Figures 14 and 15).

To decode each layer feature map into an intermediary saliency map, we adopt a recently proposed adaptive decoder (Equation 2). Exploring decoders is outside the scope of this work, but we refer the reader to recent works that discuss decoders for FLIM networks [Joao et al., 2023; Soares et al., 2024; Joao. et al., 2024].

From the saliency map of each layer $S_l = \{S_l\}_{l=1}^L$, we initialize the CA cell's states, where θ_0^0 and θ_1^0 represents background and foreground strengths, respectively, at $t = 0$. For θ_1^0 , we simply normalize S_l within $[0, 1]$ and set cells' foreground strengths $\theta_1^0(p)$. However, the FLIM encoder may have pooling operations with strides larger than 1 for both datasets. If necessary, we upsample the saliency map S_l (bilinear upsampling) to the same size as the input image, as image color/intensity are employed to guide CA's evolution, and the loss of edge information through downsampling operations may degrade CA's performance.

Initializing the background strengths, θ_0^0 , is more challenging, and hence our method considers two approaches given the dataset at hand. The first approach assumes that FLIM networks are good at detection and that the CA's can improve salience delineation while eliminating false positives. Hence, we initialize θ_0^0 as the complement of saliency maps (S_l) posterior to a dilation operation of radius 10. Accordingly, we are able to evaluate CA's capability of correctly evolving to fit tumor and parasite eggs. Figure 6 shows an example where no prior assumption can be made about where the salient object (parasite eggs) may appear. For example, background priors [Qin et al., 2018] are unsuitable, as eggs can be spotted at

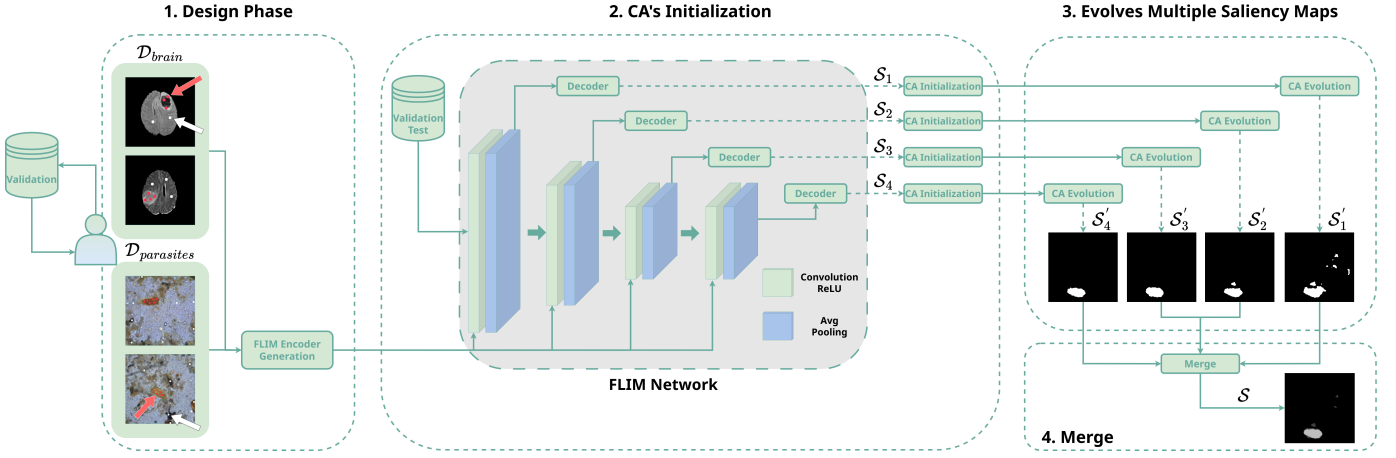


Fig. 4: Multi-Level Cellular Automata for FLIM networks (example for a 4-layer FLIM Network): (1) Users iteratively select training images and define FLIM-Encoder architecture. (2) During inference, images enter the encoder, and features decode into intermediary saliency maps, initializing CA cells. (3) Multi-level saliency maps evolve from this initialization, and (4) merge into a final saliency.

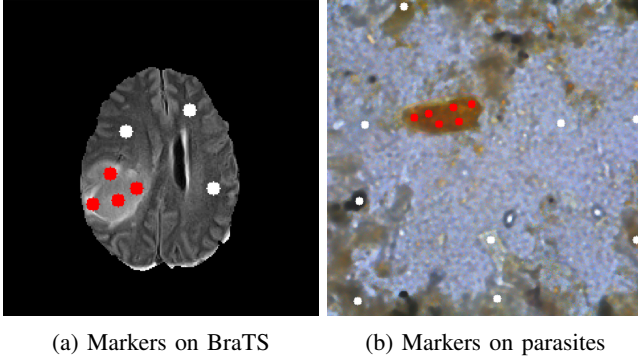


Fig. 5: Examples of user annotations: red markers indicate tumors or parasite eggs; white markers show healthy brain tissue, background, or debris.

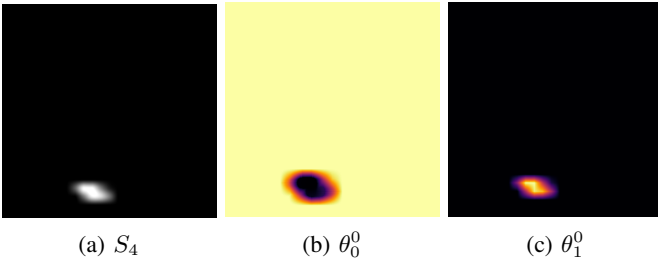


Fig. 6: Example of initialization procedure for parasite eggs detection. FLIM-Network saliency from layer 4 (a) initializes background (b) and foreground strength (c).

image borders.

The second approach concerns applications where a reasonable assumption about the background can be made. In such cases, we initialize the background strength as $\theta_0^0 \leftarrow 1$ based on a mask. Figure 6 exemplifies such an example, where the salient object is brain tumors. As brain tumors only appear

inside the brain, we can employ a *brain prior*, were given a brain mask, background strengths are easily defined.

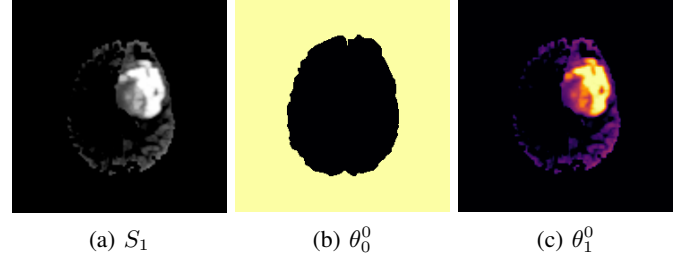


Fig. 7: Example of the initialization procedure for brain tumor detection. FLIM-Network saliency from layer 1 (a) initializes background (b) and foreground strength (c).

Lastly, we need to initialize the label map LM at $t = 0$, where we set $LM(p) \leftarrow 1$, if $\theta_1^0(p) > 0$, and 0 otherwise. The described initialization procedure is the same as that applied to each layer, and once it is done, we evolve each CA (one for each encoder level).

C. CA's evolution

The CA's evolution is detailed in Algorithm 1, where the same algorithm details the evolution of each CA. Hence, what we describe here is the same as that applied to each CA; the only difference is how they were initialized. Once the cell's state is set, we evolve each CA state (*i.e.*, foreground and background) until convergence is reached — when there is little to no update on a given evolution step.

The evolution happens based on a Moore Neighborhood (8-neighbors), where we took inspiration from the tumor cut algorithm proposed by Hamamci et al. [2012]. We evolve for each object label, $ol \in \{0, 1\}$, background and foreground, respectively. The execution occurs first for $ol = 1$ (foreground) and later for $ol = 0$ (background).

Algorithm 1 Cellular Automata initialized by FLIM

Input:

\mathbf{I} - input image, where $\hat{\mathbf{I}} = (D, \mathbf{I})$;
 θ - Cells strength, initialized by FLIM, where $\hat{\theta} = (D, \theta)$;
 ol - object label being evolved (0 — 1, background — foreground);
 LM - Cells' current label, where $\hat{LM} = (D, LM)$.

Output: Evolved Cells' strength.

```

1: procedure CA( $\mathbf{I}, \theta_{ol}^0, ol, LM$ )
2:    $t \leftarrow 0$ 
3:    $dist \leftarrow +\infty$ 
4:   while  $dist > 10^{-8}$  do
5:      $\theta_{ol}^{t+1} \leftarrow \theta_{ol}^t$  ▷ Copy previous  $\theta$ 
6:     for  $\forall p \in D$  do
7:        $q_{max} \leftarrow \theta_{ol}^t(p)$ 
8:       for  $\forall q \in N(p)$  do ▷ Moore
9:          $q_{aux} = g(p, q) \times \theta_{ol}^t(q)$ 
10:        if  $q_{aux} > q_{max}$  then
11:           $\theta_{ol}^{t+1}(p) \leftarrow q_{aux}$ 
12:           $LM(p) \leftarrow LM(q)$ 
13:           $q_{max} \leftarrow q_{aux}$ 
14:        end if
15:      end for
16:    end for
17:     $dist \leftarrow ||\theta_{ol}^t - \theta_{ol}^{t+1}||_2 / |D_I|$ 
18:     $\theta_{ol}^t \leftarrow \theta_{ol}^{t+1}$  ▷ Update step
19:     $t \leftarrow t + 1$ 
20:  end while
21:  return  $\theta_{ol}^t$ 
22: end procedure

```

Given an input image I , initial strength θ_{ol}^0 , and label map LM , the algorithm begins by initializing a control variable $dist$ (Line 3) used for convergence detection in the main loop (Line 3). In each iteration, the future cell's strength θ_{ol}^{t+1} is copied from the current strength (Line 5) to keep track of unconquered cells.

The core evolution process (Lines 6-16) evolves each cell p in the domain. For each cell, the algorithm sets the q_{max} as the current strength of p (Line 7) and then evaluates all neighboring pixels q in the Moore neighborhood (Line 8). For each neighbor, it calculates q_{aux} as the product of a similarity function $g(p, q)$ and the neighbor's current strength $\theta_{ol}^t(q)$ (Line 9). If this calculated value exceeds the current maximum strength q_{max} (Line 9), the cell p is conquered (Lines 11-13).

After processing all pixels, the algorithm computes the L2-norm between current and future strengths normalized by domain size to measure convergence (Line 17). The current strength θ_{ol}^t is updated with the future strength (Line 18), and the iteration counter t is incremented (Line 19). This process continues until the convergence is reached ($dist$ distance falls below 10^{-8} , indicating convergence).

The similarity function $g(p, q)$ is computed according to Equation 3, which incorporates image features (intensity/color) to guide the evolution process. The β parameter smooths the weight reduction during evolution if evolving inside the object (see Section IV-C), which means that a lower value will cause foreground regions to leak. In contrast, higher values will penalize the saliency map on edge regions, as cells will lose strength fast and may not fit correctly to the object border.

$$g(p, q) = \begin{cases} e^{\beta ||\vec{I}(p) - \vec{I}(q)||_2}, & \text{if evolving object} \\ e^{-||\vec{I}(p) - \vec{I}(q)||_2}, & \text{otherwise,} \end{cases} \quad (3)$$

Once convergence is reached, combining foreground (θ_1^t) and background (θ_0^t) strengths generates a object probability map O_l (Equation 4), and we define a binary saliency map S_l^t by thresholding O_l . Figure 8 exemplifies the whole evolution pipeline, where from FLIM-Network initialization, we evolve the foreground and background strengths (middle column), which enables us to compute the object probability map (O_l) and thresholding the parasite egg.

$$O_l(p) = \frac{\ln(\theta_0^t(p))}{\ln(\theta_0^t(p)) + \ln(\theta_1^t(p))} \quad (4)$$

As exemplified in Figure 4, the CA evolution is performed for each FLIM-Network level, producing L saliency maps, which explores multi-level hierarchical features. Through multiple initializations, we now have an ensemble of complementary saliency maps that can be combined to produce a more robust final segmentation result.

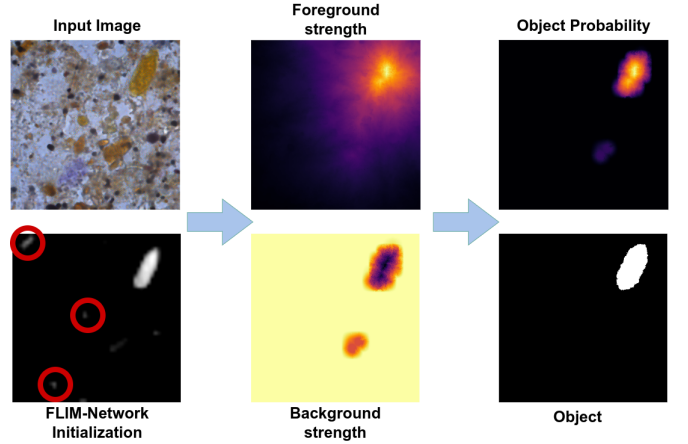


Fig. 8: The first column shows the input image and FLIM initialization to CA. The middle column shows the evolved foreground and background strengths. The last column shows the object probability map and binary saliency. Our method evolves correctly even with false positives (red circles).

D. Merge multiple saliency maps

Given the improved saliency maps from CA Evolution, we want to merge them into a single final saliency map. As each evolved saliency corresponds to a hierarchical layer in our FLIM network, we want to leverage the best of each saliency

without increasing the method’s complexity. The inputs of the merging network are all evolved saliency maps $S'_l = \{S'_l\}_{l=1}^L$ and the input image, which guides the merge procedure. During the initialization phase, if necessary, we upsample the saliencies to the size of the input image; then, the evolved saliencies are the same size. We designed a straightforward and efficient fully convolutional neural network to merge all evolved saliency maps into a final saliency map (guided by the input image). Figures 9 show an example of such a merge network for a 4-layer FLIM network.

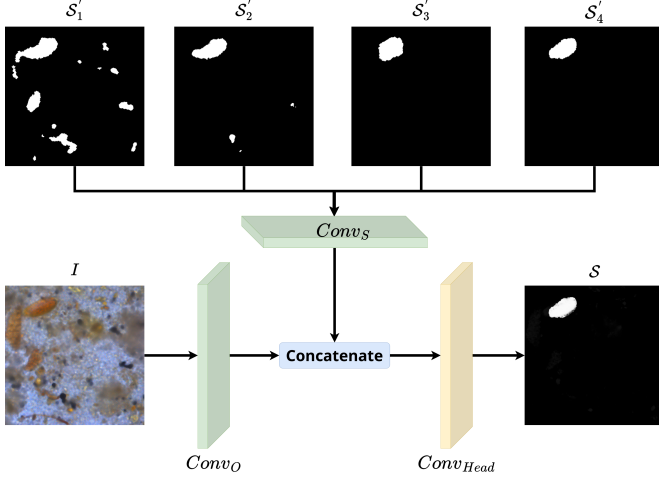


Fig. 9: Merging multiple saliency maps from CAs supervised by input image.

The simplicity of this merging network is well suited to our problem, where we face two main challenges: learning from few images (3-4) and learning from imperfect saliency maps. We want to combine multiple-level saliency maps, merging correct regions and eliminating incorrect ones. We train this simple model for 2000 epochs, with a learning rate of $(1e-2)$, Adam optimizer, and l1 regularization (with $\lambda = 1e-3$); we also employed the cosine annealing scheduler to take advantage of lower learning rates and learning resets. The key aspect of our training procedure was aggressive augmentations, where we employed random crop, horizontal and vertical flip, rotation, sharpness, affine, and perspective transformations. Our implementation guarantees that the same augmentations are applied to the multiple-saliencies and input image.

The network is composed of 3 convolutional filters. First, a single $3 \times 3 \times c$ kernel ($Conv_O$), in which c is the number of channels of the input image (e.g., 3 for RGB images and 1 for gray-scale ones), extracts features from the input image (I). In parallel, a single $3 \times 3 \times L$ kernel ($Conv_S$) combines the L saliency maps. Both convolutions generate a single-channel feature map, to which we apply a sigmoid activation function. The two feature maps are concatenated and fed to $Conv_{head}$, which generates the final saliency map with a point-wise convolution of $1 \times 1 \times 2$ followed by a sigmoid.

At this stage, our approach resembles an ensemble of CAs initialized through multi-level features, namely a multi-level

CA. We can replicate the proposed method for multi-channel images, focusing on scenarios where collecting large datasets and pixel-wisely annotating images is problematic.

IV. EXPERIMENTAL SETUP

This section details the setup to validate the proposed method on two challenging datasets. We will guide the reader through building a FLIM network and its integration into the multi-level CA approach, discussing how to initialize, evolve, and merge the saliency maps. Additionally, this section also presents the SOD models used for comparison with our method, as well as the evaluation metrics employed for assessment.

A. Designing a FLIM Network

We choose two medical datasets to validate the proposed method: the BraTS 2021 [Baid et al., 2021] for brain tumor segmentation and a private dataset of parasite eggs. For BraTS, we extract 2D axial slices of brain tumors (T2-FLAIR), three slices for every image (given the tumor volume, we select axial indexes representing the median, 1st and 3rd quartile). For parasites, images were collected through a method (DAPI) developed in our lab focused on the automated diagnosis of human and pet parasites [Suzuki et al., 2013].

The problem of parasites is intrinsically related to the deep SOD problems, mainly inference time and annotation cost. Given an input slide, DAPI performs the screening and processing of around 2000 images with four million pixels each, segmenting and identifying objects of interest, where the whole pipeline must take less than 5 minutes. Recent works show that deep neural networks improve the diagnosis of gastrointestinal parasites in humans, cats, and dogs [Osaku et al., 2020; de Melo Joao et al., 2023]. However, given the need for less than 5-minute processing times, applying those methods without considerably increasing costs is impossible. Moreover, annotating the volume of ground-truth data required for training is both timely and financially expensive. Hence, we need lighter networks, and at the same time, we want to take advantage of weak annotations.

With the goal of broader validation of our method, we chose to explore the BraTS 2D dataset, as it enables us to assess our image in a different domain (MRI images), with grayscale images, and with a more heterogeneous dataset (multi-institutional dataset).

Once datasets are prepared, we split them into three splits, each composed of validation and test subsets, following a 50/50 ratio. For parasites, after the splitting, we also filter only images that contain parasites. Hence, we end up with the following configurations of splits: 336/296, 308/324, and 326/306 (validation/test images). For the brain tumor dataset, the three splits have 1882/1882 validation and test images, as we guarantee during dataset construction that all images hold tumor regions.

The next step is to generate the architecture of the FLIM Encoder. As we previously detailed in Section II-C, there are two steps where the FLIM methodology performs filter

reduction and, hence, harnesses user control. First, when the number of filters extracted from one image (from all markers) is larger than the upper limit of filters set for each image, and second, if the total number of filters learned is larger than the number of filters specified in the convolutional layer. To avoid those reductions, we took the following decisions:

- 1) We only use disks as marks (*i.e.*, user clicks, see Figure 5), so we control the exact position that generates filters;
- 2) Each marker generates four filters;
- 3) The specified number of filters for each convolutional layer is 200, and given the number of selected images and drawn markers, we never surpass this number.

We proceed to image selection after specifying these requirements in the FLIM network. First, one image is randomly chosen from the validation subset, and we draw markers on descriptive and discriminative regions (Figure 5 exemplifies those markers). One can see this procedure as weak supervision once there is no need for a densely annotated ground truth, and filters are learned directly from marked regions. After a FLIM encoder is created, we apply the adaptive decoder described in Equation 1, which is empirically configured with $A_1 = 0.1$ and $A_2 = 0.2$ for the area thresholds. Then, we compute metrics (F-Score, Dice, MAE) for all validation data and select a new image for annotation based on the worst predictions, increasing the training subset. We repeat this procedure until the desired performance is achieved. It is a manual procedure, but there is parallel work on automating image selection for training [Cerqueira et al., 2024b,a].

TABLE I: FLIM Encoder for Parasites dataset (s for stride)

Layer	Conv	Activation	Pooling
1	(3×3)	ReLU	Avg $(3 \times 3 s2)$
2	(3×3)	ReLU	Avg $(3 \times 3 s2)$
3	(3×3)	ReLU	Avg $(3 \times 3 s1)$
4	(3×3)	ReLU	Avg $(3 \times 3 s1)$

A suitable architecture for CA initialization is typically achieved within 3 to 4 training images. Table I presents the encoder architecture for parasites, while Table II displays the 2D BraTS encoder architecture.

TABLE II: FLIM Encoder for BraTS 2D dataset (s for stride)

Layer	Conv	Activation	Pooling
1	(3×3)	ReLU	Max $(3 \times 3 s2)$
2	(3×3)	ReLU	Max $(3 \times 3 s1)$
3	(3×3)	ReLU	Max $(3 \times 3 s1)$

As the number of filters depends on the number of markers on training images, they differ slightly across splits. On parasites, we have 121, 147, and 141 filters for the three splits, respectively. The number of filters across splits for brain tumors is 60, 48, and 68. All layers within each split maintain the same number of filters for both datasets.

We develop the FLIM-Encoder architectures empirically, based upon an experimental analysis. A deeper study of designing encoders is outside our scope since our goal was to validate multi-level CA initialization through FLIM. Once

this step is finished, we have a convolutional encoder (FLIM-based) ready for inference and initializing CA's cell states. By combining these encoder with our adaptive decoder, the same across all feature levels, we have a FLIM network.

The FLIM network consists of different numbers of layers for each dataset. Our method is evaluated using a 4-layer FLIM network for parasites and a 3-layer FLIM network for brain tumors. For the parasites, the saliency maps are represented as $[S_1, S_2, S_3, S_4]$, as illustrated in the method pipeline. For brain tumors, we generate three saliency maps $[S_1, S_2, S_3]$ from the 3-layer convolutional encoder.

B. Multi-level CA parametrization and execution

Given the two defined datasets and the extracted saliency maps, both datasets' foreground strengths are initialized identically. However, as depicted in Section III-B, the brain dataset allows us to initialize the background strength based on a prior (*brain prior*), which assumes that background strengths are the maximum value outside the brain. Then, for BraTS, we used the brain mask, and the background strengths are easily defined as $\theta_0^0 \leftarrow 0$ (inside the brain) and $\theta_0^0 \leftarrow 1$ (outside the brain). For parasites, posterior to a dilation operation of radius 10. For initialization examples, see Figures 6 and 7.

After all CA are initialized, we evolve them according to the Algorithm 1. To experiment with CA algorithm parametrization, we explored the validation data, and once we had selected its parameters (*i.e.*, different thresholding on brain images), we used our test subsets to assess our results. Since we are dealing with gray-scale and RGB images, the first configuration specific for each dataset is the β parameter in Equation 3. For the brain, we smooth evolution when evolving in the foreground ($LM(q) = 1$), and if $I_1(p) > I_1(q)$ (gray-scale images), given the fact that the tumor core is darker than the surrounding tumor (edematous tissue). For parasites, we also verify if evolving on the foreground and the Euclidean distance in LAB color space ($\|\tilde{I}(p) - \tilde{I}(q)\|_2 < 0.2$). For both datasets, when smoothing $\beta = 0.6$.

Once evolution converged, we now have multiple object probability maps, $O_l = \{O_l\}_{l=1}^L$, which must be thresholded to generate the improved saliency maps $S'_l = \{S'_l\}_{l=1}^L$. Thresholding the object probability map required special attention. For parasites, S'_l is defined by pixels with $O_l(p) > Otsu(O_l)$ (Figure 8 exemplifies the evolution end-to-end). For brain tumors, a different approach was required. Rather than using Otsu thresholding on the probability map, a histogram-based statistical analysis performs better. We first analyze pixel intensity distributions within the brain mask, focusing on the upper-intensity spectrum (top 10%), which enhances the detection of the characteristic peak of the whole tumor on T2-FLAIR images. After identifying this peak intensity, we compute the mean (μ) and standard deviation (σ) of intensity values within a 20% window around the peak. The final threshold is then defined as $\tau = \mu - k\sigma$, where k is a constant parameter (empirically set to $k = 2.5$). Any pixel with intensity greater than this threshold ($I(p) \geq \tau$) is classified as tumor tissue in the binary saliency map S'_l . This statistical approach better

accommodates the distinctive high-intensity characteristics of tumor regions T2-FLAIR images while adaptively adjusting to image-specific intensity distributions.

Our final step in multi-level CA now concerns merging the improved saliency maps $S'_l = \{S'_l\}_{l=1}^L$. As shown in Figure 4, the CA evolution is performed for each FLIM-Network level, producing four saliency maps for parasite segmentation and three saliency maps for brain tumor detection, exploring multi-level hierarchical features, which now composes an ensemble of CA, or the multi-level CA, through the merging network. Through multiple initializations, we now have an ensemble of complementary saliency maps that can be combined to produce a more robust final segmentation result. The only difference between the merging network for the two chosen datasets happens in the input filters, where the input convolution has $c = 3$ (RGB) and $L = 4$ for parasites and $c = 1$ (gray-scale) and $L = 3$ for brain tumors.

C. Evaluation Metrics & Benchmark

To evaluate the efficacy of multi-level CA for FLIM-Networks, we employed the following metrics: F-Score, μ WF, Dice, e-measure, s-measure, and MAE. All metrics, except for MAE, range from 0% to 100%, with higher values indicating better saliency maps.

The F-Score and μ WF metrics assess the quality of the binarized saliency map (threshold set as 0.5) by combining precision and recall [Achanta et al., 2009; Margolin et al., 2014]. Following the literature, we empirically set $\beta^2 = 0.3$ to give more emphasis on precision. Similarly, Dice measures the overlapping ratio between the binary saliency map and the binary ground truth, making it particularly effective for evaluating improvements in edge regions [Qin et al., 2019]. The s-measure [Fan et al., 2017] evaluates the structural similarity between the normalized saliency map and the binary ground truth (with $\alpha = 0.5$). After subtracting their global means, the e-measure [Fan et al., 2018] quantifies the correlation between the binary saliency map and ground truth. The e-measure metric simultaneously accounts for global statistics and local pixel-level matching. MAE [Perazzi et al., 2012] computes the pixel-wise absolute difference between the normalized saliency map and the binary ground-truth mask, directly measuring prediction deviation. Before metrics computing, we filter components by area: [1000, 9000] for parasites and [100, 20000] for brain.

Leveraging the metrics above, we then compare our model to three recent lightweight models: SAMNet [Liu et al., 2021], MSCNet [Lin et al., 2022], and MEANet [Liang and Luo, 2024]; and to two recent heavier models: BasNet [Qin et al., 2019] and U²-Net [Qin et al., 2020]. Our goal is to benchmark our model against deep SOD, comparing the performance of those models under constrained scenarios where annotated data are scarce. Therefore, we fine-tune those models on the same training images employed in the FLIM design phase (3-4 images). Remarkably, FLIM networks are significantly smaller than lightweight networks.

To fine-tune the models, we utilized the weights released by the authors. For BasNet and U², trained on the augmented DUTs-TR dataset (21,106 images), we fine-tuned with a lower learning rate (1e-4) and additional augmentations (vertical/horizontal flips, rotation, color jittering, Gaussian noise). For lightweight models, we used the authors' pretrained models and code, where even the backbone had been previously fine-tuned on ImageNet.

V. RESULTS & DISCUSSION

In this study, we present an investigation of a novel initialization method for CA while also exploring an ensemble of multi-level CAs for two datasets: parasite eggs and brain tumors. We want a saliency map on parasites that correctly locates and delineates a parasite egg. As we process T2-FLAIR images for brain tumors, we aim to detect and delineate the whole tumor (a hyperintense signal on T2-FLAIR sequences).

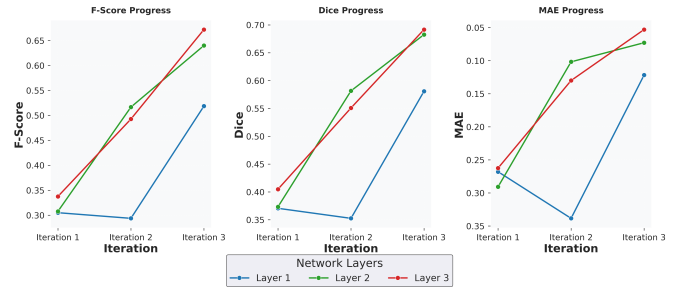


Fig. 10: Metrics improvement on validation data across FLIM design. We start with one training image and at each iteration we add one more image.

The first step in enabling the proposed method involves selecting a random image to train an initial FLIM encoder. By decoding extracted features, we can compute metrics for all validation data, where images with bad performance are candidates for increasing the training data. Figure 10 exemplifies this procedure for building the FLIM encoder for brain tumor split 1. We see significant improvements over the analyzed metrics across each iteration. For instance, at iteration 1, with one image, F-Score values are around 0.3 to 0.35 for layers 1 to 3. However, as we add one more image training image, there is a slight decrease in F-Score for layer 1, while we see an increase of around 0.15 for layers 2 and 3. An improvement for all layers is observable once we add a third training image. Since layers 2 and 3 show metric values around 0.65 at this iteration, we assume the FLIM encoder is suitable for CA initialization, and the training procedure is done. This iterative procedure has two key benefits:

- 1) It allows choosing the right amount of training data;
- 2) It also allows the identification of the suitable network architecture for the given problem. For instance, if the performance of layer 3 is worse than that of layer 2, we can modify our FLIM encoder to have only two convolutional layers.

Once the design phase is done, we will have a FLIM network, and we can run inferences. We first extract each

validation and test image’s features, decode them into an intermediary saliency map (one for each encoder level), and then initialize our multiple CAs, where evolutions happen until convergence. Tables III and V summarize our results on test sets (average and standard deviation across splits) for parasites and BraTS 2d, respectively.

Table III demonstrates that multi-level CA significantly enhances saliency across all layers of parasites. Comparing intermediary saliency to CA output, we observed improvements in F-Score (by 2.8-13.7%), μ WF (by 26.7-43.4%), Dice coefficient (by 26.2-41.3%), e-measure (by 22.4-34.4%), and s-measure (by 28.1-37.4%). For MAE, our method reduced error values by 0.091-0.31, significantly improving pixel-wise accuracy. These results confirm that our approach enhances precision, recall, delineation quality, structural similarity, and correlation between predictions and ground-truth masks while reducing overall error. Our method exhibits greater consistency, as demonstrated by lower standard deviation values across all metrics.

The improvements across all layers yield suitable saliency maps for merging, which can be characterized as a Multi-Level CA or a CA’s ensemble. On the merged column on Table III, we visualize that by a simple network composed of 3 convolutional filters, we can generate a saliency map that combines multiple saliencies into a better one. Except for MAE, the merged saliency surpasses metrics on all layers. Nevertheless, even for MAE, the average metric is closer to the better layer (layers 2 and 3).

The merging network’s potential is also confirmed when applied to FLIM-Network saliencies. Even before CA, the merge network can improve the saliency map (e.g., 17.5% improvement on Dice). Besides exploring each saliency map’s best features, the merge network also facilitates inferences using FLIM networks. When extracting multi-level saliency maps, we need to verify which layer yields better saliency (e.g., we have a higher average dice on layer 3). Merging multiple saliencies eliminates this need. Also, as inference time is a requisite, these three convolutions can be converted to simple arithmetic operations executed pixel-wise once.

When we analyze a split, the same conclusions arise. Figure 11 shows metrics distribution (μ WF) across each layer, and after merging, for split 1. An expressive improvement in the metric average and quartiles is observed, which ensures better stability after running CA. More interestingly, we see the FLIM key feature to extract features and, consequently, saliencies, which shows a delineation-to-detection tendency. Initial layers have more evident edges that fit ground-truth masks but may present many false positives, which results in the higher standard deviation of layer 1. As we go deeper into the network, edges get blurrier. However, false positives tend to disappear and, consequently, are better for CA initialization, as the evolution tends to correct edge regions if it has lower confidence (i.e., blurrier). This behavior is evident in image 14 (14b-14e).

Table IV then compares merged metrics (both FLIM and FLIM_CA) with lightweight and conventional deep SOD. We

see that FLIM merged saliencies are comparable to both deep SOD methods, while FLIM_CA outperforms all methods. Moreover, lightweight models (MSCNet and MEANet) also outperform deeper models, which shows that under constrained scenarios (few training images), the optimization over a more complex surface (more model parameters) is problematic, even with models pretrained on larger datasets (i.e., DUTS-TR or ImageNet). As previously stated, lightweights target scenarios with limited computing resources, but when compared to FLIM-Networks, models are yet larger. Take, for instance, MSCNet, with 3.6M parameters, against a FLIM network with 400k (11.11%) parameters for split 1, which substantially outperforms MSCNet when applying multi-level CA. FLIM_MCA is a post-processing operation that does not increase the parameter count.

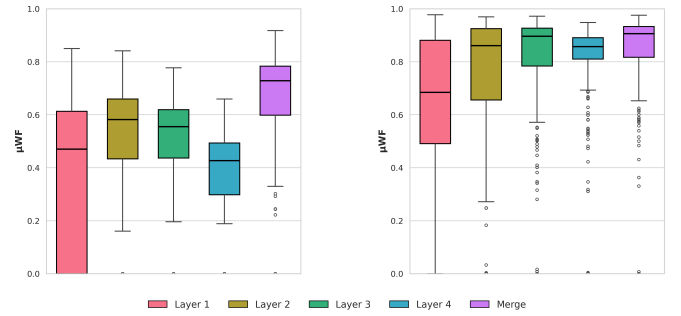


Fig. 11: Metrics distribution across all layers (parasites data) on split 1. FLIM distribution on the left against FLIM_MCA on the right.

Moving our analysis to the problem of detecting saliency, which stands for whole tumors on the BraTS 2D dataset, the same steps were adopted to design the FLIM encoder. Despite holding grayscale images, the BraTS 2D dataset is challenging, given data heterogeneity (as the original 3D dataset is multi-institutional) and the necessity for domain adaptation during fine-tuning (pretrained models were developed on RGB images).

Contrary to parasite experiments, except for F-Score and MAE, Table V shows improvements on BraTS 2D only on the first and second layers. Nevertheless, gains in metrics are substantial: F-Score (by 5.6-10.1%), μ WF (by 2.2-6.5%), Dice coefficient (by 2.5-7.1%), e-measure (by 4.8-11.5%), and s-measure (by 6.1-13%), and on MAE we see an error reduction of 0.035 to 0.122. An analysis of a split’s distribution (Figure 12) shows that the method saturates when it reaches layer 3. However, for all other layers, there is an improvement in both average metric value and stability (standard deviation), while some outliers remain (dots on the image). Still, we see a higher standard deviation across all layers for every split, which we believe is strongly related to data heterogeneity; hence, selecting more representative images for the FLIM encoder design is important.

Furthermore, as we see saturation on layer 3, experimenting with minor modifications to architecture design is also important. Examples are adding stride on layers 2 and 3 (pooling)

TABLE III: Metrics for parasites on test.

Metric	Model	Layer_1	Layer_2	Layer_3	Layer_4	Merged
F-Score (\uparrow)	FLIM	0.467 \pm 0.053	0.690 \pm 0.022	0.726 \pm 0.020	0.602 \pm 0.027	0.821 \pm 0.010
	FLIM_MCA	0.604 \pm 0.019	0.718 \pm 0.020	0.780 \pm 0.011	0.779 \pm 0.011	0.834 \pm 0.017
μ WF (\uparrow)	FLIM	0.310 \pm 0.042	0.472 \pm 0.019	0.480 \pm 0.019	0.350 \pm 0.018	0.660 \pm 0.011
	FLIM_MCA	0.632 \pm 0.021	0.739 \pm 0.017	0.795 \pm 0.009	0.784 \pm 0.011	0.816 \pm 0.017
Dice (\uparrow)	FLIM	0.322 \pm 0.043	0.494 \pm 0.020	0.505 \pm 0.020	0.378 \pm 0.019	0.680 \pm 0.010
	FLIM_MCA	0.657 \pm 0.021	0.756 \pm 0.015	0.805 \pm 0.007	0.791 \pm 0.009	0.823 \pm 0.015
e-measure (\uparrow)	FLIM	0.518 \pm 0.058	0.688 \pm 0.015	0.701 \pm 0.011	0.598 \pm 0.013	0.848 \pm 0.014
	FLIM_MCA	0.862 \pm 0.005	0.912 \pm 0.007	0.935 \pm 0.007	0.936 \pm 0.008	0.940 \pm 0.004
s-measure (\uparrow)	FLIM	0.404 \pm 0.043	0.558 \pm 0.014	0.584 \pm 0.011	0.517 \pm 0.012	0.756 \pm 0.012
	FLIM_MCA	0.778 \pm 0.010	0.840 \pm 0.009	0.867 \pm 0.006	0.850 \pm 0.006	0.879 \pm 0.008
MAE (\downarrow)	FLIM	0.337 \pm 0.061	0.146 \pm 0.013	0.110 \pm 0.006	0.168 \pm 0.014	0.057 \pm 0.007
	FLIM_MCA	0.030 \pm 0.001	0.019 \pm 0.001	0.019 \pm 0.002	0.032 \pm 0.003	0.031 \pm 0.008

TABLE IV: Benchmark on parasites test set (FLIM Metrics stands for merged model).

Model	F-Score (\uparrow)	μ WF (\uparrow)	Dice (\uparrow)	e-measure (\uparrow)	s-measure (\uparrow)	MAE (\downarrow)
SAMNet	0.518 \pm 0.209	0.431 \pm 0.262	0.440 \pm 0.256	0.516 \pm 0.276	0.478 \pm 0.257	0.418 \pm 0.242
MSCNet	0.730 \pm 0.032	0.695 \pm 0.009	0.709 \pm 0.008	0.854 \pm 0.017	0.775 \pm 0.009	0.086 \pm 0.023
MEANet	0.715 \pm 0.039	0.655 \pm 0.034	0.666 \pm 0.034	0.797 \pm 0.044	0.733 \pm 0.035	0.150 \pm 0.047
FLIM	0.821 \pm 0.010	0.660 \pm 0.011	0.680 \pm 0.010	0.848 \pm 0.014	0.756 \pm 0.012	0.057 \pm 0.007
FLIM_MCA	0.834 \pm 0.017	0.816 \pm 0.017	0.823 \pm 0.015	0.940 \pm 0.004	0.879 \pm 0.008	0.031 \pm 0.008
BasNet	0.701 \pm 0.118	0.654 \pm 0.128	0.663 \pm 0.126	0.786 \pm 0.111	0.737 \pm 0.109	0.155 \pm 0.094
U ² -Net	0.687 \pm 0.085	0.617 \pm 0.089	0.631 \pm 0.089	0.760 \pm 0.074	0.716 \pm 0.074	0.158 \pm 0.062

TABLE V: Metrics for BraTS 2D on test set.

Metric	Model	Layer_1	Layer_2	Layer_3	Merged
F-Score (\uparrow)	FLIM	0.516 \pm 0.015	0.633 \pm 0.022	0.673 \pm 0.016	0.699 \pm 0.034
	FLIM_MCA	0.617 \pm 0.007	0.718 \pm 0.013	0.730 \pm 0.015	0.712 \pm 0.005
μ WF (\uparrow)	FLIM	0.577 \pm 0.021	0.675 \pm 0.020	0.688 \pm 0.011	0.697 \pm 0.013
	FLIM_MCA	0.642 \pm 0.012	0.698 \pm 0.012	0.656 \pm 0.025	0.710 \pm 0.013
Dice (\uparrow)	FLIM	0.574 \pm 0.021	0.675 \pm 0.018	0.689 \pm 0.011	0.700 \pm 0.015
	FLIM_MCA	0.645 \pm 0.012	0.701 \pm 0.011	0.664 \pm 0.024	0.713 \pm 0.011
e-measure (\uparrow)	FLIM	0.707 \pm 0.035	0.822 \pm 0.018	0.848 \pm 0.015	0.841 \pm 0.018
	FLIM_MCA	0.822 \pm 0.001	0.870 \pm 0.005	0.833 \pm 0.020	0.877 \pm 0.007
s-measure (\uparrow)	FLIM	0.624 \pm 0.033	0.726 \pm 0.013	0.756 \pm 0.012	0.771 \pm 0.017
	FLIM_MCA	0.754 \pm 0.006	0.787 \pm 0.008	0.757 \pm 0.017	0.799 \pm 0.009
MAE (\downarrow)	FLIM	0.166 \pm 0.057	0.082 \pm 0.012	0.069 \pm 0.016	0.075 \pm 0.021
	FLIM_MCA	0.044 \pm 0.001	0.027 \pm 0.002	0.034 \pm 0.004	0.032 \pm 0.001

TABLE VI: Benchmark on BraTS 2D test set (FLIM Metrics stands for merged model).

Model	F-Score (\uparrow)	μ WF (\uparrow)	Dice (\uparrow)	e-measure (\uparrow)	s-measure (\uparrow)	MAE (\downarrow)
SAMNet	0.000 \pm 0.000	0.000 \pm 0.000	0.000 \pm 0.000	0.000 \pm 0.000	0.000 \pm 0.000	1.000 \pm 0.000
MSCNet	0.431 \pm 0.012	0.234 \pm 0.003	0.269 \pm 0.001	0.459 \pm 0.028	0.509 \pm 0.003	0.158 \pm 0.017
MEANet	0.118 \pm 0.020	0.116 \pm 0.013	0.123 \pm 0.014	0.680 \pm 0.054	0.446 \pm 0.036	0.149 \pm 0.078
FLIM	0.699 \pm 0.034	0.697 \pm 0.013	0.700 \pm 0.015	0.841 \pm 0.018	0.771 \pm 0.017	0.075 \pm 0.021
FLIM_MCA	0.712 \pm 0.005	0.710 \pm 0.013	0.713 \pm 0.011	0.877 \pm 0.007	0.799 \pm 0.009	0.032 \pm 0.001
BasNet	0.775 \pm 0.022	0.751 \pm 0.020	0.756 \pm 0.019	0.880 \pm 0.028	0.830 \pm 0.011	0.024 \pm 0.007
U ² -Net	0.728 \pm 0.026	0.684 \pm 0.017	0.692 \pm 0.015	0.834 \pm 0.033	0.785 \pm 0.012	0.037 \pm 0.012

and experimenting with average pooling. As overconfidence in edge regions causes the CA to leak the background into the foreground, blurrier edges would be of great importance and have the potential to overcome saturation. Also, a significant difference from our previous work is how we threshold the object probability map [Salvagnini et al., 2024]. Instead of a fixed threshold, we employed a histogram-based threshold, significantly improving our results. We omitted those results for conciseness but experimented with fixed thresholds, the Otsu threshold computed using the brain mask, and different

histogram-based thresholds. In summary, all approaches generated saliencies worse than FLIM. It emphasizes the key role of thresholding for tumor salient object detection, and there is room for improvement.

When we merge the multi-level saliencies, the same improvements observed on parasites stand out (see also Figure 12). However, on FLIM saliencies, for e-measure and MAE, merge statistics are closer to the best layer but do not surpass it. Merging FLIM_MCA saliencies also yields better metrics, except for F-Score and MAE, which are comparable to the best

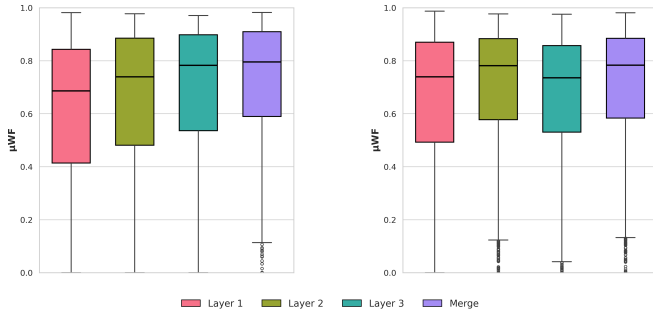


Fig. 12: Metrics distribution across all layers (BraTS 2D data) on split 2. FLIM distribution on the left against FLIM_MCA on the right.

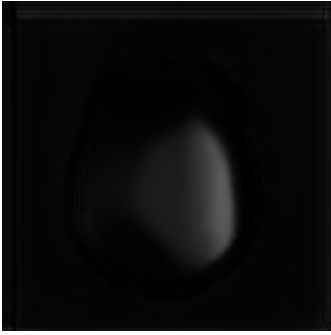


Fig. 13: Sample of SAMNet's predictions.

layer. Both results show that in the worst scenario, merging yields comparable results. Merging results on both datasets lay down the floor for further experiments with merging, as it shows that taking advantage of all layers' saliencies is possible and could improve overall results. Experiments with more complex networks, taking the proper care to avoid overfitting, have the potential to further improvements. Moreover, using the probability map instead of the binarized saliency could eliminate the necessity to compute thresholds. We tried the same merge networks using the probability map but without success.

Comparing merged results with deep SOD literature shows a different behavior than the parasites' benchmark. First, lightweight networks fail fine-tuning to a different domain — pre-trained weights were learned on RGB images — when few training images are available. All networks fail to learn, even with our efforts to experiment with different learning rates to reach the best performance. SAMNet could not predict saliency maps, which detect tumors correctly, and saliency maps had all values below the threshold for metric computation. Thus, SAMNet has the worst metrics possible.

Distinctly from lightweight methods, deeper networks learned a different domain (gray-scale images), in which BasNet and U²-Net generate better saliency maps than all lightweight models. BasNet has the best results. Nevertheless, FLIM and FLIM_MCA showed competitive results compared to BasNet, significantly outperforming U²-Net on most met-

rics.

From a qualitative perspective, Figures 14 and 15 summarize our observations from a detailed analysis of the method outputs. Both images present the FLIM output (CA initialization), the CA output, and the merged saliency. We also provide two examples: one demonstrating a successful case and the other illustrating a problematic one. As a blue line, we see ground-truth edges.

Figure 14 (14a-14j) shows visualize what we have already discussed so far. First, on layer 1, we see much noise (false positives) while the parasite's egg itself is darker than some false positives. Deeper saliency values on the egg surpass false positive values, while false positives disappear. Finally, we see the blurrier characteristic on the last layer and only two false-positive components. Despite the noise of initialization, we see that both the initialization and evolution procedures are robust and can eliminate most false positives (dark debris at the bottom of the image). On the last layer, CA eliminates all false positives. The merged saliency has a single false positive component, and the only remaining (which appears on layers 1 to 3) has a lower saliency value and is eliminated in the thresholding step. Supporting our discussion on the method's robustness against false positives, Figures 14k to 14t show how initialization and evolution eliminate most of the wrong saliencies. We clearly see that the darker component will be thresholded out on merged saliency. However, it shows a limitation of our method on evolution when lower saliency values are employed for initialization or when only a small portion of the parasite egg was salient on FLIM saliencies. The CA cannot evolve correctly to fit most parasites' eggs in such cases. A possible approach to overcome this problem is extracting components' statistics (e.g., mean LAB value on salient component) and using this description to propagate cells' strengths better.

For brain tumor examples (Figures 15a to 15h), we see that despite false positives, our method correctly fits the whole tumor, eliminating false positive values. On the brain, false positives consistently have lower values than on tumors. Furthermore, on FLIM saliencies for layer 2 and layer 3, we can spot higher saliency values outside the tumor. Nevertheless, as we initialize background strength on the brain border and evolve it into the brain, we correctly eliminate those regions. The second case shows a more problematic example, which is frequent on training data. If we analyze the input image, we can easily see that the tumor ground truth encompasses a hyper-intense region but a dark one, too. As it has intensity values similar to brain tumor tissue, FLIM saliencies also detect the dark region as a tumor, and evolution happens, leaking into the background. The leaking is more intense on deeper layers, as more regions are initialized with higher values, which justifies the FLIM_MCA degradation on the third layer.

Leaking may occur when the CA propagates foreground strength into healthy brain tissue or background regions on parasites due to incorrect initialization. More typically, when using deeper network layers (like layer 3), their saliency maps

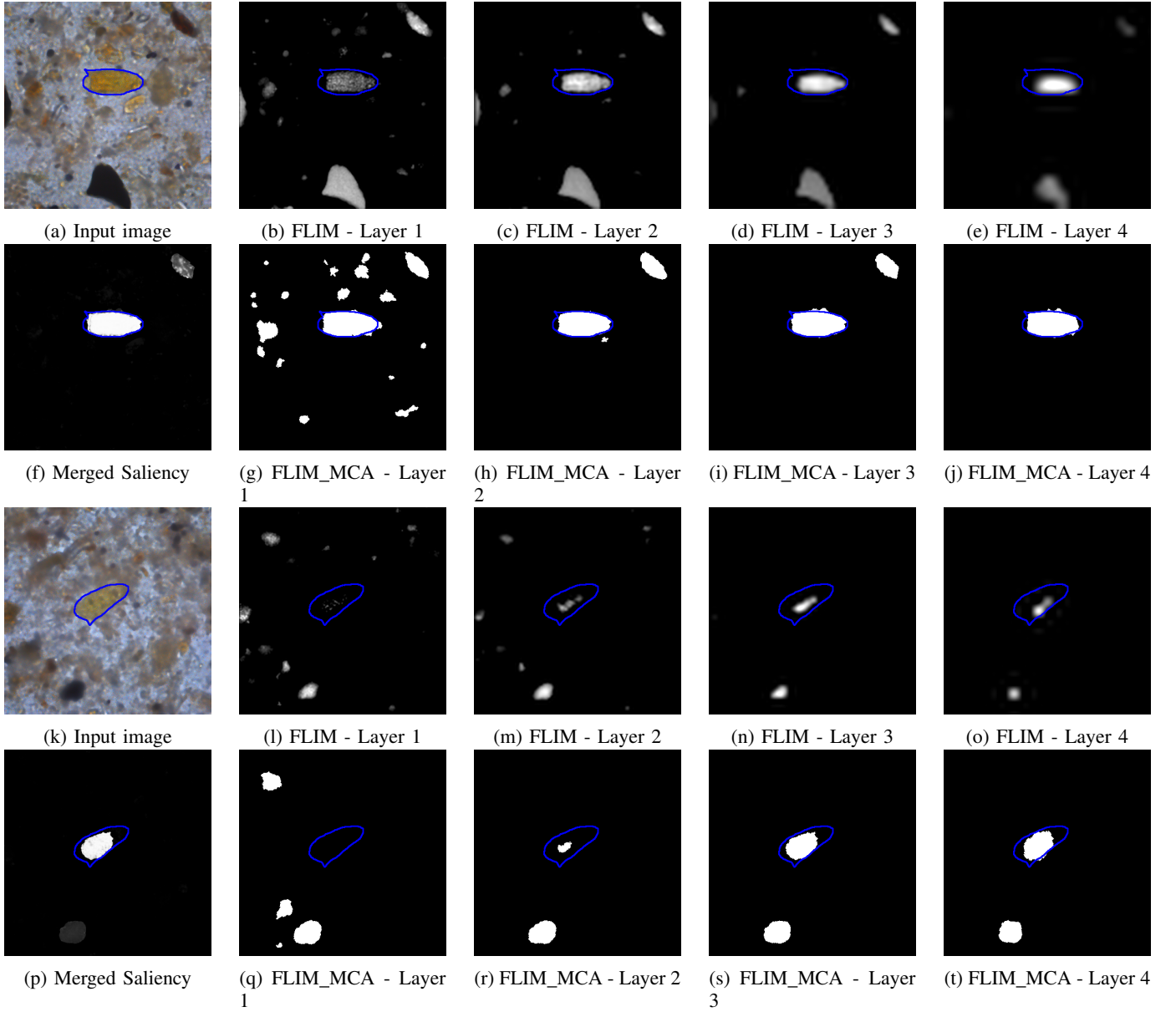


Fig. 14: Multi-level CA on parasite data. The first two rows show images with superior performance, while the bottom rows show problematic ones. The blue line represents ground-truth mask edges.

are blurrier and cover larger areas than those from earlier layers. This saliency causes healthy brain regions (hypo-intense regions in Figure 15i) to be incorrectly initialized as foreground (tumor). During evolution, these misclassified regions act as “seeds” that spread and “conquer” neighboring tissues with similar characteristics, resulting in false positives extending beyond the tumor boundaries. A possible approach for better robustness would be experimenting with different pooling (average or minimum), which could provide a better initialization. It is important to note that the ground-truth tumor masks annotated by specialists also include these hypo-intense regions (blue line on Figures 14 and 15).

From the results discussed, a conclusion arises. With a

fraction of parameters, FLIM_MCA outperforms deep SOD methods for parasites and reaches competitive performances under a more heterogeneous problem (BraTS 2D). Nevertheless, there is plenty of room for improvements in every phase of the proposed method, from image selection to decode, initialization, evolution, and merging. We also note that the implemented solution employs Open MP, where the whole pipeline (CA initialization, evolution, and merging) takes around 3s. There is significant potential to improve efficiency when working with constrained computing resources.

VI. CONCLUSION

We expanded previous work on improving the CA initialization problem by exploring knowledge distilled at different

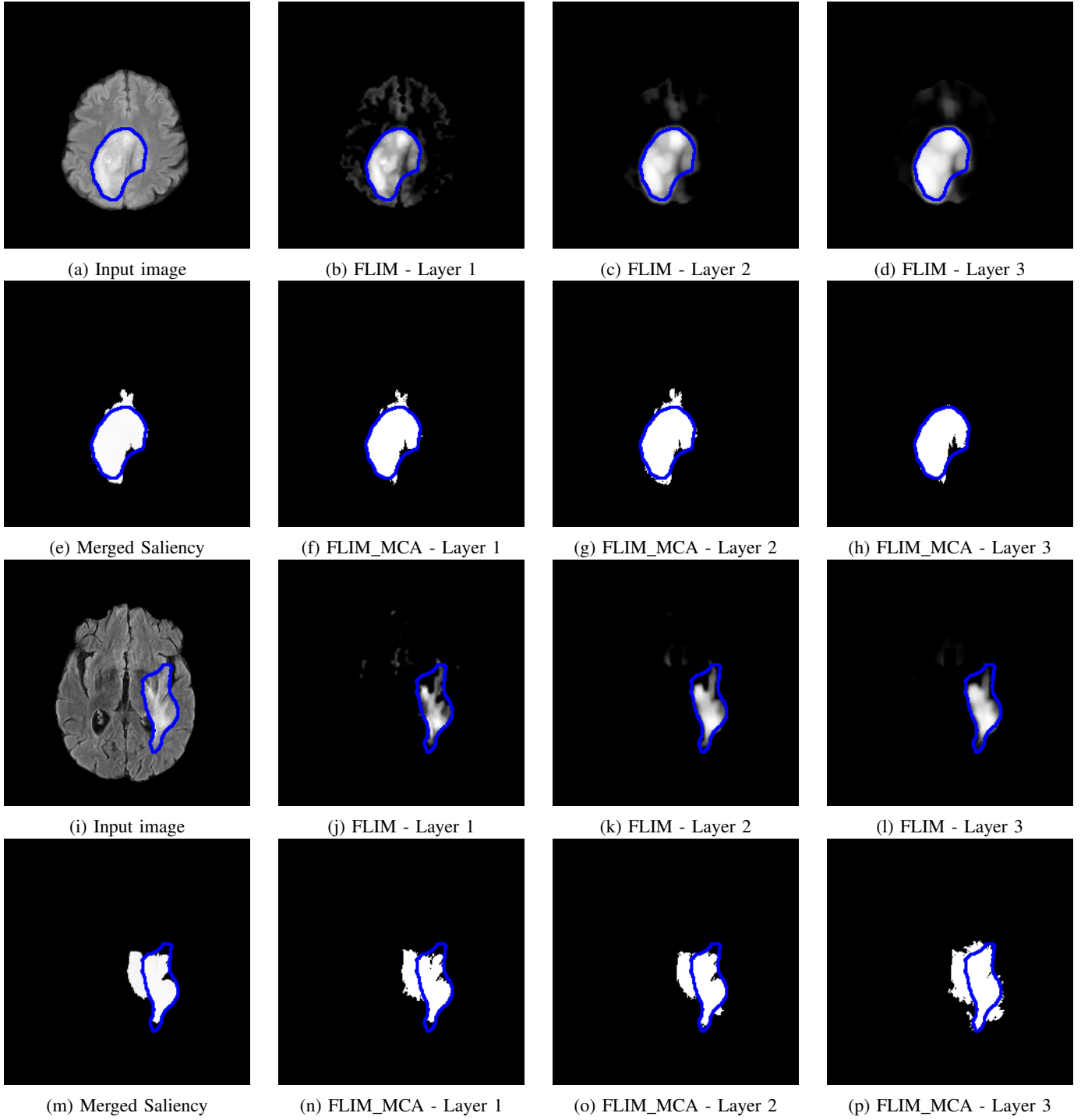


Fig. 15: Multi-level CA on BraTS 2D data. The first two rows show images with superior performance, while the bottom rows show problematic ones. The blue line represents ground-truth mask edges.

hierarchical levels of FLIM networks. CA methods have shown competitive performance, particularly in medical problems where abundant training and annotated data are challenging to obtain. While CA typically requires user interaction for every image, our approach incorporates user knowledge into a FLIM network that initializes the CA automatically. By

initializing a separate CA for each convolutional layer of the FLIM Network, we create a multi-level CA that explores a broader initialization space, consistently improving saliency at each level (up to 43.4%).

The multi-level approach generates multiple complementary saliency maps that form a CA ensemble, leveraging each

encoder level's unique characteristics — from sharp-edged features with false positives to blurrier edges with fewer false positives. Our experiments demonstrate that these saliency maps can be effectively combined using a straightforward merging network (just three convolutional filters) trained on only 3-4 images. The merging network eliminates the need to determine which network layer yields the best saliency while maintaining high performance.

Our method showed consistent cross-domain improvements when benchmarked across both public (BraTS) and private (parasite eggs detection) datasets. For parasite detection, multi-level CA outperformed all compared models (lightweight and deeper architectures). For brain tumor detection, we outperformed all lightweight models and U²-Net while achieving comparable results to BasNet - despite using only a fraction of the parameters (400k versus 3.6M in lightweight models) and requiring only 3-4 weakly-annotated training images compared to the thousands or millions used by benchmarked approaches.

As a limitation, we see the separate evolution of foreground and background CA as an additional computational overhead that could be optimized. The method also shows some performance variability across datasets, with more substantial results on parasite detection than on more heterogeneous brain tumor data. For future work, we plan to evolve a single CA instead of separate foreground and background automata, which would reduce computational overhead and simplify rule design. This approach could enable more complex cellular interactions and facilitate 3D multi-label CA development for semantic tumor segmentation - correctly evolving a CA to simultaneously segment the whole tumor, enhanced tumor, and edematous tissue, which could be tried under a clinical environment. The simplicity of our merging network offers substantial room for investigating optimal methods to combine multi-level saliency/segmentation maps. Additionally, exploring methods for smoothing border surfaces could further improve edge regions [Sompong and Wongthanavas, 2017b; Vezhnevets and Konouchine, 2005].

From an implementation perspective, our current solution leverages CPU parallelization (OpenMP); significant speed improvements are possible through GPU optimization targeting low-cost hardware suitable for real-world applications like parasitology laboratories in developing regions.

ACKNOWLEDGMENT

We thank the Eldorado Institute. Moreover, this work was financially supported by the Conselho Nacional de Desenvolvimento Científico e Tecnológico – CNPq – (407242/2021-0, 306573/2022-9, 442950/2023-3, 304711/2023-3), the Fundação de Amparo a Pesquisa do Estado de Minas Gerais – FAPEMIG – (APQ-01079-23 and APQ-05058-23), the Fundação de Amparo a Pesquisa do Estado de São Paulo – FAPESP – (2023/14427-8 and 2013/07375-0) and the Coordenação de Aperfeiçoamento de Pessoal de Nível Superior – CAPES – (STIC-AMSUD 88887.878869/2023-00).

REFERENCES

- Radhakrishna Achanta, Sheila Hemami, Francisco Estrada, and Sabine Susstrunk. Frequency-tuned salient region detection. In *2009 IEEE Conference on Computer Vision and Pattern Recognition*, pages 1597–1604, 2009. doi: 10.1109/CVPR.2009.5206596.
- Radhakrishna Achanta, Appu Shaji, Kevin Smith, Aurelien Lucchi, Pascal Fua, and Sabine Süssstrunk. Slic superpixels compared to state-of-the-art superpixel methods. *IEEE Transactions on Pattern Analysis and Machine Intelligence*, 34(11):2274–2282, 2012. doi: 10.1109/TPAMI.2012.120.
- Achanta, Radhakrishna, Estrada, Francisco, Wils, Patricia, and Süssstrunk, Sabine. Salient region detection and segmentation. In Gasteratos, Antonios, Vincze, Markus, and Tsotsos, John K., editors, *Computer Vision Systems*, pages 66–75, Berlin, Heidelberg, 2008. Springer Berlin Heidelberg. ISBN 978-3-540-79547-6. doi: 10.1007/978-3-540-79547-6_7.
- Ujjwal Baid et al. The RSNA-ASNR-MICCAI BraTS 2021 Benchmark on Brain Tumor Segmentation and Radiogenomic Classification. *arXiv e-prints*, art. arXiv:2107.02314, July 2021. doi: 10.48550/arXiv.2107.02314.
- Gunilla Borgefors. Distance transformations in arbitrary dimensions. *Computer Vision, Graphics, and Image Processing*, 27(3):321–345, 1984. ISSN 0734-189X. doi: https://doi.org/10.1016/0734-189X(84)90035-5. URL https://www.sciencedirect.com/science/article/pii/0734189X84900355.
- Ali Borji, Ming-Ming Cheng, Qibin Hou, Huaizu Jiang, and Jia Li. Salient object detection: A survey. *Computational Visual Media*, 5(2):117–150, 2019. doi: 10.1007/s41095-019-0149-9.
- Matheus A. Cerqueira, Flávia Sprenger, Bernardo C. A. Teixeira, and Alexandre X. Falcão. Interactive image selection and training for brain tumor segmentation network. In *2024 46th Annual International Conference of the IEEE Engineering in Medicine and Biology Society (EMBC)*, pages 1–4, 2024a. doi: 10.1109/EMBC53108.2024.10781962.
- Matheus A. Cerqueira, Flávia Sprenger, Bernardo C. A. Teixeira, Silvio Jamil F. Guimarães, and Alexandre X. Falcão. Interactive ground-truth-free image selection for flim segmentation encoders. In *2024 37th SIBGRAPI Conference on Graphics, Patterns and Images (SIBGRAPI)*, pages 1–6, 2024b. doi: 10.1109/SIBGRAPI62404.2024.10716300.
- Alexandros Chariton, Nikolaos Passalis, and Anastasios Tefas. Bag-of-features-based knowledge distillation for lightweight convolutional neural networks. In *2022 IEEE International Conference on Image Processing (ICIP)*, pages 1541–1545, 2022. doi: 10.1109/ICIP46576.2022.9897390.
- Fanghui Chen, Shouliang Li, Jiale Han, Fengyuan Ren, and Zhen Yang. Review of lightweight deep convolutional neural networks. *Archives of Computational Methods in Engineering*, 31(4):1915–1937, May 2024. ISSN 1886-1784. doi: 10.1007/s11831-023-10032-z. URL https://doi.org/10.1007/s11831-023-10032-z.
- Ming-Ming Cheng, Niloy J. Mitra, Xiaolei Huang, Philip

- H. S. Torr, and Shi-Min Hu. Global contrast based salient region detection. *IEEE Transactions on Pattern Analysis and Machine Intelligence*, 37(3):569–582, 2015a. doi: 10.1109/TPAMI.2014.2345401.
- Ming-Ming Cheng, Niloy J. Mitra, Xiaolei Huang, Philip H. S. Torr, and Shi-Min Hu. Global contrast based salient region detection. *IEEE Transactions on Pattern Analysis and Machine Intelligence*, 37(3):569–582, 2015b. doi: 10.1109/TPAMI.2014.2345401.
- Xiangxiang Chu, Bo Zhang, and Ruijun Xu. Moga: Searching beyond mobilenetv3. In *ICASSP 2020 - 2020 IEEE International Conference on Acoustics, Speech and Signal Processing (ICASSP)*, pages 4042–4046, 2020. doi: 10.1109/ICASSP40776.2020.9054428.
- Matthew Cook et al. Universality in elementary cellular automata. *Complex systems*, 15(1):1–40, 2004. doi: 10.25088/ComplexSystems.15.1.1.
- Leonardo de Melo Joao, Letícia Rodrigues Proença, Saulo Hudson Nery Loiola, Sandra Valéria Inácio, Bianca Martins dos Santos, Stefany Laryssa Rosa, Felipe Augusto Soares, Vitória Castilho Stefano, Daniel Osaku, Celso Tetsuo Nagase Suzuki, Katia Denise Saraiva Bresciani, Jancarlo Ferreira Gomes, and Alexandre Xavier Falcão. Toward automating the diagnosis of gastrointestinal parasites in cats and dogs. *Computers in Biology and Medicine*, page 107203, 2023. doi: 10.1016/j.compbimed.2023.107203.
- Italos Estilon de Souza and Alexandre Xavier Falcão. Learning cnn filters from user-drawn image markers for coconut-tree image classification. *IEEE Geoscience and Remote Sensing Letters*, 19:1–5, 2022. doi: 10.1109/LGRS.2020.3020098.
- Italos Estilon de Souza, Barbara C. Benato, and Alexandre Xavier Falcão. Feature learning from image markers for object delineation. In *2020 33rd SIBGRAPI Conference on Graphics, Patterns and Images (SIBGRAPI)*, pages 116–123, 2020. doi: 10.1109/SIBGRAPI51738.2020.00024.
- Deng-Ping Fan, Ming-Ming Cheng, Yun Liu, Tao Li, and Ali Borji. Structure-measure: A new way to evaluate foreground maps. In *2017 IEEE International Conference on Computer Vision (ICCV)*, pages 4558–4567, 2017. doi: 10.1109/ICCV.2017.487.
- Deng-Ping Fan, Cheng Gong, Yang Cao, Bo Ren, Ming-Ming Cheng, and Ali Borji. Enhanced-alignment measure for binary foreground map evaluation. In *Proceedings of the 27th International Joint Conference on Artificial Intelligence, IJCAI’18*, page 698–704. AAAI Press, 2018. ISBN 9780999241127. doi: 10.5555/3304415.3304515.
- Pedro F Felzenszwalb and Daniel P Huttenlocher. Efficient graph-based image segmentation. *International journal of computer vision*, 59:167–181, 2004. doi: 10.1023/B:VISI.0000022288.19776.77.
- Andac Hamamci, Nadir Kucuk, Kutlay Karaman, Kayihan Engin, and Gozde Unal. Tumor-cut: Segmentation of brain tumors on contrast enhanced mr images for radiosurgery applications. *IEEE Transactions on Medical Imaging*, 31(3):790–804, 2012. doi: 10.1109/TMI.2011.2181857.
- Gonzalo Hernández and Hans J. Herrmann. Cellular automata for elementary image enhancement. *Graphical Models and Image Processing*, 58(1):82–89, 1996. ISSN 1077-3169. doi: <https://doi.org/10.1006/gmip.1996.0006>. URL <https://www.sciencedirect.com/science/article/pii/S1077316996900064>.
- Hu Huang, Ping Liu, Yanzhao Wang, Tongchi Zhou, Boyang Qu, Aimin Tao, and Hao Zhang. Multi-feature aggregation network for salient object detection. *Signal, Image and Video Processing*, 17(4):1043–1051, June 2023. ISSN 1863-1711. doi: 10.1007/s11760-022-02310-3. URL <https://doi.org/10.1007/s11760-022-02310-3>.
- Mingzhong Huang, Yan Liu, Lijie Zhao, and Guogang Wang. A lightweight deep neural network model and its applications based on channel pruning and group vector quantization. *Neural Computing and Applications*, 36(10):5333–5346, Apr 2024. ISSN 1433-3058. doi: 10.1007/s00521-023-09332-z. URL <https://doi.org/10.1007/s00521-023-09332-z>.
- L. Itti, C. Koch, and E. Niebur. A model of saliency-based visual attention for rapid scene analysis. *IEEE Transactions on Pattern Analysis and Machine Intelligence*, 20(11):1254–1259, 1998. doi: 10.1109/34.730558.
- Leonardo Joao., Matheus Cerqueira., Barbara Benato., and Alexandre Falcao. Understanding marker-based normalization for flim networks. In *Proceedings of the 19th International Joint Conference on Computer Vision, Imaging and Computer Graphics Theory and Applications - Volume 2: VISAPP*, pages 612–623. INSTICC, SciTePress, 2024. ISBN 978-989-758-679-8. doi: 10.5220/0012385900003660.
- Leonardo de Melo Joao, Bianca Martins dos Santos, Silvio Jamil Ferzoli Guimaraes, Jancarlo Ferreira Gomes, Ewa Kijak, Alexandre Xavier Falcao, et al. A flyweight cnn with adaptive decoder for schistosoma mansoni egg detection. *arXiv preprint arXiv:2306.14840*, 2023. doi: 10.48550/arXiv.2306.14840.
- Claude Kauffmann and Nicolas Piché. Seeded nd medical image segmentation by cellular automaton on gpu. *International Journal of Computer Assisted Radiology and Surgery*, 5(3):251–262, 5 2010. ISSN 1861-6429. doi: 10.1007/s11548-009-0392-0. URL <https://doi.org/10.1007/s11548-009-0392-0>.
- Guanbin Li and Yizhou Yu. Visual saliency based on multi-scale deep features. In *2015 IEEE Conference on Computer Vision and Pattern Recognition (CVPR)*, pages 5455–5463, 2015. doi: 10.1109/CVPR.2015.7299184.
- Yin Li, Xiaodi Hou, Christof Koch, James M. Rehg, and Alan L. Yuille. The secrets of salient object segmentation. In *2014 IEEE Conference on Computer Vision and Pattern Recognition*, pages 280–287, 2014. doi: 10.1109/CVPR.2014.43.
- Bocheng Liang and Huilan Luo. Meanet: An effective and lightweight solution for salient object detection in optical remote sensing images. *Expert Systems with Applications*, 238:121778, 2024. ISSN 0957-4174. doi: <https://doi.org/10.1016/j.eswa.2023.121778>. URL <https://www.sciencedirect.com/science/article/pii/S0957417423001778>.

- com/science/article/pii/S0957417423022807.
- Yuhan Lin, Han Sun, Ningzhong Liu, Yetong Bian, Jun Cen, and Huiyu Zhou. A lightweight multi-scale context network for salient object detection in optical remote sensing images. In *2022 26th International Conference on Pattern Recognition (ICPR)*, pages 238–244, 2022. doi: 10.1109/ICPR56361.2022.9956350.
- Feng Liu and Michael Gleicher. Region enhanced scale-invariant saliency detection. In *2006 IEEE International Conference on Multimedia and Expo*, pages 1477–1480, 2006. doi: 10.1109/ICME.2006.262821.
- Nian Liu and Junwei Han. Dhsnet: Deep hierarchical saliency network for salient object detection. In *2016 IEEE Conference on Computer Vision and Pattern Recognition (CVPR)*, pages 678–686, 2016. doi: 10.1109/CVPR.2016.80.
- Tie Liu, Jian Sun, Nan-Ning Zheng, Xiaoou Tang, and Heung-Yeung Shum. Learning to detect a salient object. In *2007 IEEE Conference on Computer Vision and Pattern Recognition*, pages 1–8, 2007a. doi: 10.1109/CVPR.2007.383047.
- Tie Liu, Jian Sun, Nan-Ning Zheng, Xiaoou Tang, and Heung-Yeung Shum. Learning to detect a salient object. In *2007 IEEE Conference on Computer Vision and Pattern Recognition*, pages 1–8, 2007b. doi: 10.1109/CVPR.2007.383047.
- Yun Liu, Xin-Yu Zhang, Jia-Wang Bian, Le Zhang, and Ming-Ming Cheng. Samnet: Stereoscopically attentive multi-scale network for lightweight salient object detection. *IEEE Transactions on Image Processing*, 30:3804–3814, 2021. doi: 10.1109/TIP.2021.3065239.
- Yu-Fei Ma and Hong-Jiang Zhang. Contrast-based image attention analysis by using fuzzy growing. In *Proceedings of the Eleventh ACM International Conference on Multimedia*, MULTIMEDIA '03, page 374–381, New York, NY, USA, 2003. Association for Computing Machinery. ISBN 1581137222. doi: 10.1145/957013.957094. URL <https://doi.org/10.1145/957013.957094>.
- Ran Margolin, Lihi Zelnik-Manor, and Ayellet Tal. How to evaluate foreground maps. In *2014 IEEE Conference on Computer Vision and Pattern Recognition*, pages 248–255, 2014. doi: 10.1109/CVPR.2014.39.
- Alexandru-Ion Marinescu, Zoltan Balint, Laura-Silvia Diosan, and Anca-Mirela Andreica. Unsupervised and fully autonomous 3d medical image segmentation based on grow cut. In *2018 20th International Symposium on Symbolic and Numeric Algorithms for Scientific Computing (SYNASC)*, pages 401–408, 2018. doi: 10.1109/SYNASC.2018.00068.
- Vida Movahedi and James H. Elder. Design and perceptual validation of performance measures for salient object segmentation. In *2010 IEEE Computer Society Conference on Computer Vision and Pattern Recognition - Workshops*, pages 49–56, 2010. doi: 10.1109/CVPRW.2010.5543739.
- D. Osaku, C.F. Cuba, C.T.N. Suzuki, J.F. Gomes, and A.X. Falcão. Automated diagnosis of intestinal parasites: A new hybrid approach and its benefits. *Computers in Biology and Medicine*, 123:103917, 2020. doi: 10.1016/j.compbiomed.2020.103917.
- Federico Perazzi, Philipp Krähenbühl, Yael Pritch, and Alexander Hornung. Saliency filters: Contrast based filtering for salient region detection. In *2012 IEEE Conference on Computer Vision and Pattern Recognition*, pages 733–740, 2012. doi: 10.1109/CVPR.2012.6247743.
- Anh-Huy Phan, Konstantin Sobolev, Konstantin Sozykin, Dmitry Ermilov, Julia Gusak, Petr Tichavský, Valeriy Glukhov, Ivan Oseledets, and Andrzej Cichocki. Stable low-rank tensor decomposition for compression of convolutional neural network. In Andrea Vedaldi, Horst Bischof, Thomas Brox, and Jan-Michael Frahm, editors, *Computer Vision – ECCV 2020*, pages 522–539, Cham, 2020. Springer International Publishing. ISBN 978-3-030-58526-6. doi: 10.1007/978-3-030-58526-6_31.
- Xuebin Qin, Zichen Zhang, Chenyang Huang, Chao Gao, Masood Dehghan, and Martin Jagersand. Basnet: Boundary-aware salient object detection. In *2019 IEEE/CVF Conference on Computer Vision and Pattern Recognition (CVPR)*, pages 7471–7481, 2019. doi: 10.1109/CVPR.2019.00766.
- Xuebin Qin, Zichen Zhang, Chenyang Huang, Masood Dehghan, Osmar R. Zaiane, and Martin Jagersand. U2-net: Going deeper with nested u-structure for salient object detection. *Pattern Recognition*, 106:107404, 2020. ISSN 0031-3203. doi: <https://doi.org/10.1016/j.patcog.2020.107404>. URL <https://www.sciencedirect.com/science/article/pii/S0031320320302077>.
- Yao Qin, Huchuan Lu, Yiqun Xu, and He Wang. Saliency detection via cellular automata. In *2015 IEEE Conference on Computer Vision and Pattern Recognition (CVPR)*, pages 110–119, 2015. doi: 10.1109/CVPR.2015.7298606.
- Yao Qin, Mengyang Feng, Huchuan Lu, and Garrison W. Cottrell. Hierarchical cellular automata for visual saliency. *International Journal of Computer Vision*, 126(7):751–770, Jul 2018. ISSN 1573-1405. doi: 10.1007/s11263-017-1062-2.
- Paul L. Rosin. A simple method for detecting salient regions. *Pattern Recognition*, 42(11):2363–2371, 2009. ISSN 0031-3203. doi: 10.1016/j.patcog.2009.04.021. URL <https://www.sciencedirect.com/science/article/pii/S0031320309001629>.
- P.L. Rosin. Training cellular automata for image processing. *IEEE Transactions on Image Processing*, 15(7):2076–2087, 2006. doi: 10.1109/TIP.2006.877040.
- Felipe Crispim R. Salvagnini, Jancarlo F. Gomes, Cid A. N. Santos, Silvio Jamil F. Guimarães, and Alexandre X. Falcão. Improving flim-based salient object detection networks with cellular automata. In *2024 37th SIBGRAPI Conference on Graphics, Patterns and Images (SIBGRAPI)*, pages 1–6, 2024. doi: 10.1109/SIBGRAPI62404.2024.10716266.
- Mark Sandler, Andrew Howard, Menglong Zhu, Andrey Zhmoginov, and Liang-Chieh Chen. Mobilenetv2: Inverted residuals and linear bottlenecks. In *IEEE conference on computer vision and pattern recognition*, pages 4510–4520, 2018. doi: 10.1109/CVPR.2018.00474.
- Evan Shelhamer, Jonathan Long, and Trevor Darrell. Fully convolutional networks for semantic segmentation. *IEEE Transactions on Pattern Analysis and Machine Intelligence*, 39(4):640–651, 2017. doi: 10.1109/TPAMI.2016.2572683.

- Gilson Junior Soares, Matheus Abrantes Cerqueira, Silvio Jamil F. Guimaraes, Jancarlo F. Gomes, and Alexandre X. Falcão. Adaptive decoders for flim-based salient object detection networks. In *2024 37th SIBGRAPI Conference on Graphics, Patterns and Images (SIBGRAPI)*, pages 1–6, 2024. doi: 10.1109/SIBGRAPI62404.2024.10716333.
- Chaiyanan Sompong and Sartra Wongthanavas. An efficient brain tumor segmentation based on cellular automata and improved tumor-cut algorithm. *Expert Systems with Applications*, 72:231–244, 2017a. ISSN 0957-4174. doi: <https://doi.org/10.1016/j.eswa.2016.10.064>. URL <https://www.sciencedirect.com/science/article/pii/S0957417416305772>.
- Chaiyanan Sompong and Sartra Wongthanavas. An efficient brain tumor segmentation based on cellular automata and improved tumor-cut algorithm. *Expert Systems with Applications*, 72:231–244, 2017b. ISSN 0957-4174. doi: <https://doi.org/10.1016/j.eswa.2016.10.064>. URL <https://www.sciencedirect.com/science/article/pii/S0957417416305772>.
- Celso T. N. Suzuki, Jancarlo F. Gomes, Alexandre X. Falcão, João P. Papa, and Sumie Hoshino-Shimizu. Automatic segmentation and classification of human intestinal parasites from microscopy images. *IEEE Transactions on Biomedical Engineering*, 60(3):803–812, 2013. doi: 10.1109/TBME.2012.2187204.
- Na Tong, Huchuan Lu, Ying Zhang, and Xiang Ruan. Salient object detection via global and local cues. *Pattern Recognition*, 48(10):3258–3267, 2015. ISSN 0031-3203. doi: <https://doi.org/10.1016/j.patcog.2014.12.005>. URL <https://www.sciencedirect.com/science/article/pii/S0031320314004932>. Discriminative Feature Learning from Big Data for Visual Recognition.
- Vladimir Vezhnevets and Vadim Konouchine. Growcut: Interactive multi-label nd image segmentation by cellular automata. In *proc. of Graphicon*, volume 1, pages 150–156. Citeseer, 2005.
- John von Neumann. The general and logical theory of automata. In *Cerebral mechanisms in behavior*, pages 1–41, 1951.
- Lijun Wang, Huchuan Lu, Xiang Ruan, and Ming-Hsuan Yang. Deep networks for saliency detection via local estimation and global search. In *2015 IEEE Conference on Computer Vision and Pattern Recognition (CVPR)*, pages 3183–3192, 2015. doi: 10.1109/CVPR.2015.7298938.
- Lijun Wang, Huchuan Lu, Yifan Wang, Mengyang Feng, Dong Wang, Baocai Yin, and Xiang Ruan. Learning to detect salient objects with image-level supervision. In *2017 IEEE Conference on Computer Vision and Pattern Recognition (CVPR)*, pages 3796–3805, 2017. doi: 10.1109/CVPR.2017.404.
- Meng Wang, Janusz Konrad, Prakash Ishwar, Kevin Jing, and Henry Rowley. Image saliency: From intrinsic to extrinsic context. In *CVPR 2011*, pages 417–424, 2011. doi: 10.1109/CVPR.2011.5995743.
- Wenguan Wang, Qiuxia Lai, Huazhu Fu, Jianbing Shen, Haibin Ling, and Ruigang Yang. Salient object detection in the deep learning era: An in-depth survey. *IEEE Transactions on Pattern Analysis and Machine Intelligence*, 44(6):3239–3259, 2022. doi: 10.1109/TPAMI.2021.3051099.
- Xiuwenxin Wang, Siyue Yu, Eng Gee Lim, and ML Dennis Wong. Salient object detection: a mini review. *Frontiers in Signal Processing*, 4:1356793, 2024. doi: 10.3389/frsip.2024.1356793.
- Qiong Yan, Li Xu, Jianping Shi, and Jiaya Jia. Hierarchical saliency detection. In *2013 IEEE Conference on Computer Vision and Pattern Recognition*, pages 1155–1162, 2013. doi: 10.1109/CVPR.2013.153.
- Qiaoning Yang, Jiahao Zheng, and Juan Chen. Multilevel diverse feature aggregation network for salient object detection. *Neurocomputing*, 628:129648, 2025. ISSN 0925-2312. doi: <https://doi.org/10.1016/j.neucom.2025.129648>. URL <https://www.sciencedirect.com/science/article/pii/S0925231225003200>.
- Rui Zhao, Wanli Ouyang, Hongsheng Li, and Xiaogang Wang. Saliency detection by multi-context deep learning. In *2015 IEEE Conference on Computer Vision and Pattern Recognition (CVPR)*, pages 1265–1274, 2015. doi: 10.1109/CVPR.2015.7298731.
- Ge Zhu, Lei Wang, and Jinping Tang. Learning discriminative context for salient object detection. *Engineering Applications of Artificial Intelligence*, 131:107820, 2024. ISSN 0952-1976. doi: <https://doi.org/10.1016/j.engappai.2023.107820>. URL <https://www.sciencedirect.com/science/article/pii/S0952197623020043>.